

Phytolith and simulation evidence for precipitation-modulated vegetation dynamics along the East Asian monsoon margin

Nannan Li ^{a,b,c,1}, Lina Song ^{a,c,1}, Dorothy Sack ^d, Zhengyao Lu ^e, Fengling Yu ^b, Guizai Gao ^{a,c}, Dehui Li ^f, Mengzhen Li ^{a,c}, Yue Yang ^{a,c}, Yazhuo Zong ^{a,c}, Dongmei Jie ^{a,c,g,*}

^a Key Laboratory of Geographical Processes and Ecological Security in Changbai Mountains, Ministry of Education, Changchun 130024, China

^b State Key Laboratory of Marine Environmental Science, College of Ocean and Earth Sciences, Xiamen University, Xiamen 361102, China

^c Institute for Peat and Mire Research, State Environmental Protection Key Laboratory of Wetland Ecology and Vegetation Restoration, Northeast Normal University, Renmin 5268, Changchun 130024, China

^d Department of Geography, Ohio University, Athens, OH 45701, USA

^e Department of Physical Geography and Ecosystem Science, Lund University, Lund 22362, Sweden

^f College of Resources and Environment Sciences, Hebei Normal University, Shijiazhuang 050024, China

^g Key Laboratory of Vegetation Ecology, Ministry of Education, Changchun 130024, China



ARTICLE INFO

Keywords:

Phytolith
Holocene
Paleoecology
Vegetation dynamics
Peat
LPJ-GUESS

ABSTRACT

An improved understanding of past interactions between terrestrial vegetation and various forcings, such as climate change, human impact, and paleofire, is crucial for assessing impacts of future global change on terrestrial ecosystems. This study seeks to find the key factor or factors that have driven Holocene vegetation change along the East Asian monsoon margin. Several high-resolution pollen records are reviewed and new phytolith-based paleovegetation reconstructions and physical geochemical datasets are presented from a peatland in northeastern China. Using 108 modern topsoil samples as a training set, canopy cover and vegetation composition are estimated for the period since 5100 cal. yr BP. Variation partitioning analysis (VPA) is used to determine the relative importance of climate change, human impacts, and paleofire disturbance. The generalized dynamic vegetation model LPJ-GUESS is forced with climate anomaly output from an atmospheric general circulation model to simulate vegetation dynamics during the mid-Holocene and the pre-industrial era. The proxy-based estimates are compared to modelling output. Results indicate that regional tree cover varied from 10% to 40% during the past five millennia. The single-core, phytolith-based reconstructions are generally consistent with stacked tree pollen z-scores calculated from different records along the East Asian monsoon margin, implying that mid-Holocene tree cover decrease was persistent and almost synchronous over extensive areas. VPA demonstrates that long-term monsoon marginal vegetation successions were mainly caused by climate effects. Numerical modelling suggests that since the mid-Holocene the retreat of forests along the monsoon margin was primarily associated with precipitation deficits. Our investigation highlights that the precipitation associated with the East Asian monsoon system has exerted a stronger influence than the westerlies on the monsoon margin climate and vegetation change. With ongoing global change, close attention to variations in precipitation patterns and amounts should be especially helpful in efforts aimed at ecological monitoring, change prediction, and restoration.

1. Introduction

Along the margin of the East Asian monsoon, natural vegetation is dominated by forest-steppe patches instead of monsoon forest due to the

decreased influence of monsoonal precipitation (Erdős et al., 2018). Investigations focusing on the interactions between vegetation and past climate change have proposed that this forest-steppe vegetation is highly sensitive to even small climate shifts (e.g., Liu et al., 2012; Yin

* Corresponding author at: Key Laboratory of Geographical Processes and Ecological Security in Changbai Mountains, Ministry of Education, Changchun 130024, China.

E-mail address: jiedongmei@nenu.edu.cn (D. Jie).

¹ Authors that contribute equally to this paper.

et al., 2013; Hao et al., 2014; Liu et al., 2014). Numerical simulations have suggested that the forest-steppe vegetation covering the semiarid monsoon-margin lands might be replaced by grasslands under the current global warming (Lucht et al., 2006). However, projecting future vegetation change remains challenging partly because the effects that climate, topography, and anthropogenic practices have on vegetation dynamics is not fully understood (e.g., Cheng et al., 2020 and references therein). Available data on vegetation change come primarily from short-term studies and remote sensing imagery, which does not extend far back in time. The lack of direct long-term vegetation succession data makes predicting future vegetation changes in monsoon margin areas particularly difficult. Paleoecological records that are crucial for an improved understanding of the long-term interactions between vegetation dynamics and climate change, as well as human impacts, can only be acquired using geological archives (e.g., Liu and Yin, 2013; Stebich et al., 2015); Zhao et al., 2017; Wu et al., 2019).

Palynological evidence from lacustrine sediments is currently the most widely used data source for paleovegetation reconstructions of semiarid lands (e.g., Yin et al., 2013; Hao et al., 2014; Liu et al., 2014; Zhao et al., 2017). Previous studies have shown that fossil pollen assemblages from lacustrine sediments in arid and semiarid lands in China are always dominated by *Pinus*, *Betula*, *Artemisia*, and *Chenopodiaceae*, which together account for 80% of the total pollen assemblages (e.g., Zhao et al., 2009; Zhao and Yu, 2012). Dominant pollen types in such assemblages, however, are not necessarily the most abundant species in the lake basin. Studies of modern pollen-vegetation relationships have found that even when *Pinus*, *Betula*, *Artemisia*, and *Chenopodiaceae* plants are rare or absent in vegetation communities, they can still dominate the pollen assemblages (Li et al., 2000; Xu et al., 2007, 2014; Li et al., 2011). With this in mind, palynologists have interpreted the variations in the relative abundances of pollen taxa (including ratios such as AP/NAP, *Artemisia*/Chenopodiaceae) as climate indices, and have found that those interpretations agree well with documented East Asian monsoon variations (e.g., Zhao and Yu, 2012; Hao et al., 2014; Chen et al., 2015; Wen et al., 2017). Precise reconstructions of vegetation types and their successions in arid and semiarid lands, such as those in the East Asian monsoon margin, remain difficult mainly because of production, transport, representation, and identification issues with pollen, combined with the limited preservation of other biological proxies (Li et al., 2000; Xu et al., 2007, 2014; Li et al., 2011).

Phytoliths are a good alternative or complementary proxy to pollen for paleovegetation reconstructions. Because phytoliths provide paleoecological information not available through conventional pollen analysis, they hold great promise for reconstructing the paleoecology of the forest-steppe ecotone in the monsoon marginal area and will further aid in obtaining an improved understanding of the ecological response of vegetation to climate change. Unlike pollen, phytoliths remain well preserved in oxidizing conditions because they are microscopic opal-A particles ($\text{SiO}_2 \cdot n\text{H}_2\text{O}$) (Piperno, 1988; Wang and Lu, 1993). In contrast to grass pollen, which is identifiable only to the family level (Poaceae), grass phytoliths are diagnostic to the subfamily level (Twiss et al., 1969; Twiss, 1992; Barboni et al., 1999) and have thus served as an important tool for paleovegetation reconstructions that involve grasses (e.g., Alexandre et al., 1997; Barboni et al., 1999; Strömberg, 2004; Boyd, 2005; Bremond et al., 2008; Neumann et al., 2017; Li et al., 2018, 2021). The potential of phytolith analysis for specifying vegetation communities and successions in the forest-steppe ecotone is underscored by recent transect calibrations conducted with modern topsoil phytolith assemblages across northeastern China (Gao et al., 2018a, 2018b). Employing those topsoil phytolith datasets, this paper presents a new perspective on paleovegetation and paleoclimate reconstruction for the East Asian monsoon margin area.

Using radiocarbon chronologies and biotic and abiotic datasets, this research addresses the following questions: (1) How did the phytolith-reconstructed vegetation change since the mid-Holocene? (2) Are the changes observed over time in the phytolith-reconstructed plant

communities different from those based on pollen analyses? (3) What is the relative importance of climate change, human population, and paleofires on monsoon marginal vegetation dynamics, and how do the impacts of these factors change over time? (4) What is the main limiting factor that regulates vegetation dynamics in the monsoon margin? LPJ-GUESS, a state-of-the-art dynamic global vegetation model (DGVM), is used to help address this question.

2. Materials and methods

2.1. Regional setting and sample collection

The Hongshuipao (HSP) peatland ($46^{\circ}58'55.01''\text{N}$, $120^{\circ}50'47.47''\text{E}$; elevation 778 m) is located in the middle of the Greater Hinggan Mountains (Fig. 1) at the northern margin of the East Asian summer monsoon. Situated in the continental interior of upper midlatitudes, the modern climate of this region displays high seasonal variability. Winter-like conditions extend from the end of September to early May, resulting in a short growing season. Regional mean annual temperature and precipitation are -2.3°C and 441.1 mm, respectively (China Meteorological Data Service Center, 2020). The lowest mean monthly temperature (-24.8°C) occurs in January and the highest mean monthly temperature (17.1°C) occurs in July (China Meteorological Data Service Center, 2020). Precipitation in meteorological summer (June, July, August) accounts for more than 60% of the annual amount (Fig. 1B).

The regional vegetation consists of boreal broadleaf-conifer mixed forests. At elevations from 500 to 1000 m, vegetation communities display forest-grassland patching characteristics (Liu et al., 2012). South-facing slopes are drier than north-facing slopes and display shrub and herbaceous communities accompanied by scattered trees: *Padus racemosa*, *Spiraea salicifolia*, Poaceae, *Filifolium sibiricum*, etc. Shadier (north-facing) slopes support abundant broadleaf trees, such as *Quercus mongolica*, *Betula platyphylla*, *Populus Davidiana*, and *B. dahurica*, mainly due to lower evaporation rates. Meadows that are dominated by Poaceae, *Carex chinganensis*, *Saussurea salicifolia*, *Fragaria orientalis*, *Equisetum arvense*, and others, form local communities along broad river valleys. At elevations above 1000 m, plant communities are dominated by *Larix gemelini*, *Pinus sylvestris*, and *B. platyphylla* forests (Hou, 1982; Liu et al., 2012).

The Hongshuipao peatland lies in the broad valley of the Tuoxin River (Fig. 1C). The peatland vegetation consists of wetland species, such as *Carex* spp., Poaceae, *Eriophorum scheuchzeri*, *Deyeuxia angustifolia*, *B. fruticosa*, *Vaccinium uliginosum*, *Potentilla fruticosa*, and *Sphagnum* spp. In summer 2016, three parallel peat cores (HSP-1, HSP-2, and HSP-3) were collected along an east-west transect in the peatland using an Eijkelpamp peat sampler (Li et al., 2020a). Peat core HSP-2 was selected for this study (because core HSP-2 is the longest core of the three peat sections, cf. Li et al., 2020a) and processed for phytolith and geochemical analyses at 1-cm intervals. The upper 13 cm of peat core HSP-2 were not processed for analyses because of the dominance of modern plant roots.

2.2. Laboratory methods

2.2.1. Chronology, LOI, and humification quantification methods

To establish the chronological model for peat core HSP-2, radiocarbon dates were obtained from bulk peat samples because of insufficient macrofossil content. AMS¹⁴C ages were provided in conventional age before present (BP, 1950 CE), and calibrated into calendar ages using the IntCal13 calibration curve in the CALIB Rev. 7.04 program. The age-depth model was established using Bacon v2.2 in R. Details of the radiocarbon dating and age-depth model appear in Li et al. (2020a).

Loss-on-ignition (LOI) was used to determine the total organic carbon (TOC), ash, and carbonate content for each sample. For analysis, oven-dried (105°C) subsamples of approximately 1.000 g each were weighed in a crucible. Crucibles were placed in a muffle furnace

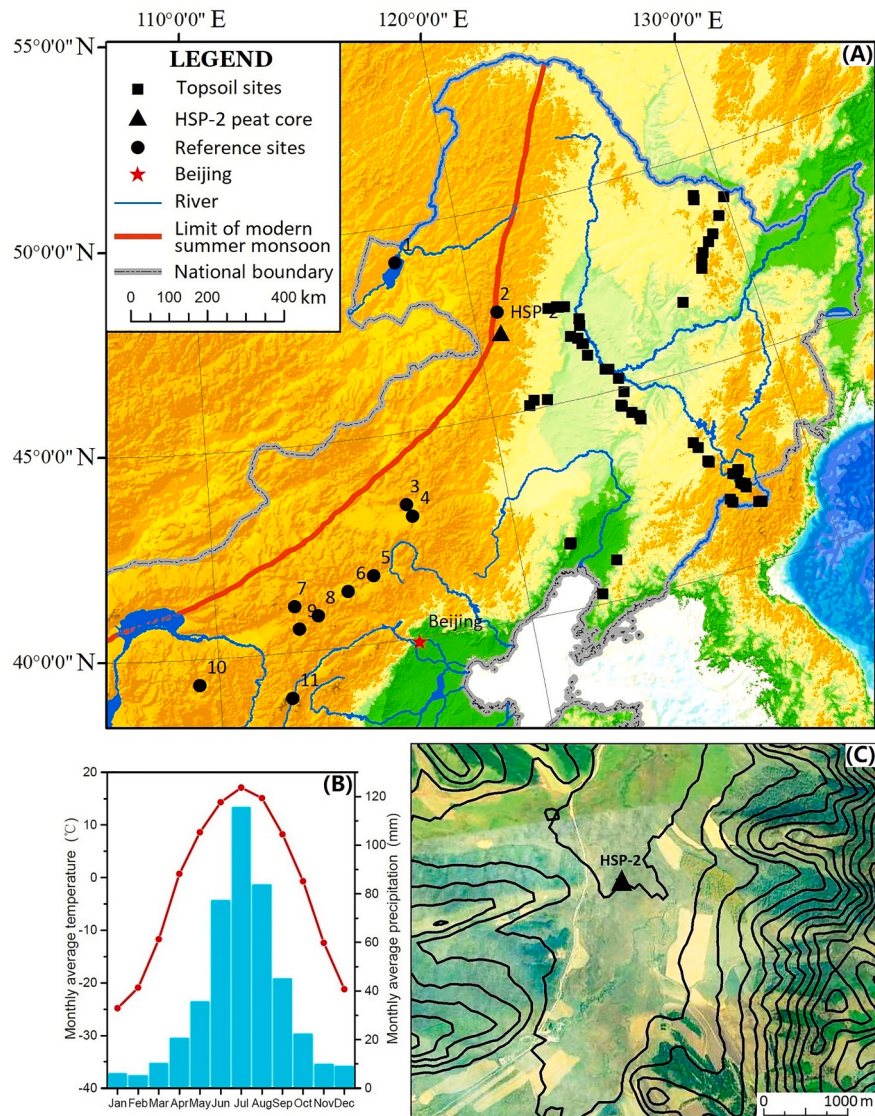


Fig. 1. (A) Investigation area and the locations of sampling and reference sites (Table 1) in China. (B) Climatic pattern for the sampling area. Diagrams show monthly averaged temperature and precipitation of A'er'shan station from 1981 to 2010 (<http://data.cma.cn/>). (C) Location of core HSP-2 in the Hongshuiapao peatland and geographical setting (contour lines were shown in black).

(SX-8–10, Taisite, China) and combusted for 12 h at 500°C. After combustion, the samples were cooled in a desiccator and weighed. The samples were then placed back into the muffle furnace and combusted at 800°C for 12 h to determine weight loss. All samples were weighed with a 0.1 mg analytical balance (BSA124S-CW, Sartorius, Germany). TOC, ash, and carbonate contents were calculated according to Li et al. (2020b).

Peat humification was determined using a modified version of the method described in Chambers et al. (2011). For each sampled interval, a 0.1000 g dry and homogenized peat subsample was weighed accurately into a 100 mL beaker. An 80 mL solution of 8% NaOH was added to the beaker and heated at 90°C for 1 h. After cooling to room temperature, the sample and solution were separated using a filter, and transferred into a 100 mL flask. The humification degree was determined from the absorbance (expressed as a percentage) of the sample solution at a wavelength of 540 nm. The measurements were performed with an SP-722 visible spectrophotometer. Analytical precision for the absorbance measurements was 0.1%.

2.2.2. Grain size analysis

Dry peat samples of approximately 0.5 g were first treated with 10%

hydrochloric acid (HCl) for 12 h to remove carbonates. After rinsing in distilled water, the residuals were treated with 30% hydrogen peroxide (H₂O₂) until the reaction ceased to remove organic matter. Next, 10 mL of 0.05 mol/L sodium hexametaphosphate ((NaPO₃)₆) was added to the mineral samples to facilitate dispersion. After a 10 min ultrasonic bath, the grain size distribution of each sample was determined with a MICROTAC S3500 particle analyzer that automatically yields the percentages of the clay-, silt-, and sand-size fractions and the median diameter over the grain size range of 0.02–2000 µm. Replicate analyses determined that the mean grain size had an analytical error of 2%. Conventional grain size parameters that describe the grain size distribution of a bulk sample (i.e., mean grain size (Mz)) were calculated by a program intrinsic to the particle analyzer. Finally, the standard deviation (SD) vs. grain size class method (Boulay et al., 2003) was employed to assemble a paleoenvironmental proxy for the peat records.

2.2.3. Phytolith extraction

Phytoliths were extracted from approximately 1 g subsamples of the cores using a modified version of the Piperno (1988) method (Wang and Lu, 1993). Each subsample was treated with 10% HCl to remove carbonates. Organic matter was removed using 65% HNO₃ in a 70°C water

Table 1
Summary of geographical information, climate, fossil pollen data from 11 Holocene lacustrine pollen records along the monsoon marginal area in northern China.

No.	Site	Long.	Lat.	Elev. (m)	MAT ($^{\circ}$ C)	MAP (mm)	Achieve type	Number of ^{14}C dates	Sampling resolution (in year)	Time span (cal. yr BP)	Carbon reservoir estimation (years)	Comment*	Reference
1	Hulun Lake	117.51	49.13	545	0.3	300	Lacustrine sediments	13	70	11,000-present	685	Modern lake	Wen et al. (2010)
2	Lake Moon	120.87	47.51	1190	3.2	500	Lacustrine sediments	21	40	20,000-present	\	Modern lake	Wu et al. (2019)
3	Dali Lake	116.60	43.26	1226	3.2	392	Lacustrine sediments	16	40	12,000-present	472	Modern lake	Wen et al. (2017)
4	Haoluku Lake	116.76	42.96	1295	1	370	Lacustrine sediments	4	200	10,500-present	\	Paleo-lake	Liu et al. (2002)
5	Lake Bayanchagan	115.21	41.65	1355	2.4	380	Lacustrine sediments	9	140	12,500-present	570	Lake dried	Jiang et al. (2006)
6	Lake Anguli Nuur	114.33	41.33	1320	3.1	350	Lacustrine sediments	7	50	10,900-present	\	Lake dried	Wang et al. (2010)
7	Lake Diaojiaohaizi	112.57	41.12	2015	0	350	Lacustrine and peaty sediments	13	80	13,300-2100**	\	Lacustrine plain	Yang (2001)
8	Lake Huangqihai	113.28	40.83	1261	4.5	360	Lacustrine sediments	15	60	8620-present	1440	Lake dried	Hao et al. (2014)
9	Daihai Lake	112.65	40.55	1221	5.1	423	Lacustrine sediments	8	40	10,250-present	360	Modern lake	Xiao et al. (2004)
10	Lake Qigai Nuur	109.37	39.37	1308	7	300	Lacustrine sediments	17	50	10,700-present	1950	Modern lake	Sun and Feng (2013)
11	Gonghai Lake	112.23	38.90	1860	6.2	468	Lacustrine sediments	25	20	14,700-present	\	Modern lake	Chen et al. (2015)

* The 'modern lake' implies the lake wasn't dried by the sampling year.

** The age-depth model is recalculated using Bacon v2.2 since the original radiocarbon dates were not calibrated.

bath. Phytoliths were extracted through heavy liquid (ZnBr_2) flotation at a density of 2.35 g/cm^3 . A tablet of *Lycopodium* spores (27,560 spores per tablet) was added to each subsample to determine the abundance of phytoliths (phytolith concentration). After cleaning, each sample was rinsed in distilled water and ethanol and placed on slides in Canada balsam for counting and storage. Phytoliths were identified mainly following the classification system used by Lu et al. (2006), Gao et al. (2018a, 2018b), and with reference to the classification systems of Twiss et al. (1969). Phytolith identification, photography, and counting (usually >300 diagnostic per sample) were performed at $600\times$ magnification using an Olympus BX53 optical microscope at Northeast Normal University. Phytoliths were named according to the International Code for Phytolith Nomenclature 2.0 (International Committee for Phytolith Taxonomy (ICPT), 2019).

2.3. Reference data source, processing, and statistical analyses

2.3.1. Reference data source

To compare the phytolith-based reconstruction with those derived from pollen analyses, 11 high-resolution Holocene pollen profiles from lakes and paleolakes were selected to construct a synthetic paleo-vegetation profile for the East Asian monsoon margin area. The location, length, time span, and relevant information about the profiles are summarized in Table 1. These reference sites were selected based on the following criteria: (1) a continuous record covering most of the Holocene without an obvious sedimentary hiatus; (2) high sampling resolution, and (3) location within or near the monsoon margin transition area. The summed tree (arboreal) pollen percentage profile for each site was used to estimate vegetation change, and all results were normalized and averaged to calculate the synthetic tree pollen profile for the entire monsoon margin area.

Phytolith assemblages and canopy cover data from 108 modern topsoil samples collected in northeastern China were used to build the quantitative transfer function between phytolith assemblages and quadrat tree coverage. The modern training dataset included topsoil samples that spanned multiple regions of varying latitude/longitude and dominant vegetation types (Gao et al., 2018a) across northeastern China (Fig. 1). This large spatial array, as well as the occurrence of multiple samples from the same bioclimatic zone, allowed for the inclusion of localized gradients of canopy conditions that may be influenced by differences in plant communities and environmental characteristics, while still maintaining a long primary gradient of canopy coverage. The location, soil type, dominant vegetation community, and phytolith percentages of these sites are fully presented and discussed in Gao et al. (2018b). Tree coverage data for each sample plot comes from Hansen et al. (2013), who averaged values from 2000 to 2012 at a spatial resolution of 30 m.

Variation partitioning was employed to estimate the relative importance of climate change, human population, and paleofires (three explanatory variables) on regulating the phytolith-based vegetation reconstructions (induced variable). The climate variables include the Hongshupao peatland physical and chemical parameters, TraCE-21 ka simulated mean annual soil moisture (0–10 cm), mean annual precipitation, and mean annual atmospheric temperature (Liu et al., 2009). Data on human population size and paleofire syntheses were taken from Xu et al. (2019) and Xu et al. (2021), respectively. Prior to variation partitioning, all data were interpolated from the original data set at constant 50-year steps using the *spline()* function in R to provide equally spaced time series.

2.3.2. Data processing and statistical analyses

Using *Lycopodium* spores as markers, absolute abundance of phytoliths (phytolith concentration) was calculated with Eq. (1),

$$C = \frac{n \times L}{l \times m} \quad (1)$$

where C is the absolute abundance of phytoliths, in the unit of grains per gram; n is the phytolith counts for each sample; L is the number of *Lycopodium* spores per tablet (L is 27,560 for this study); l is the number of *Lycopodium* spores encountered during the phytolith counting; and m (in grams) is the initial dry subsample weight for phytolith extraction.

In addition to absolute abundance, phytolith influx was calculated for the Hongshuiapao peatland from Eq. (2).

$$\text{Phytolith influx} = C \times \text{SR} \quad (2)$$

C represents the absolute phytolith abundance (grains per gram) and SR denotes the sedimentation rate (cm/yr).

Phytolith data for each sample were presented in biostratigraphic profiles using TILIA (Grimm, 1992). Biostratigraphic zones for phytolith assemblages in core HSP-2 were established by cluster analysis using constrained incremental sum of squares (CONISS) (Grimm, 1987).

Because of multiplicity and redundancy in phytolith data (Piperno, 1988), linear discriminant analysis (LDA) was employed on the fossil phytolith assemblages to reconstruct regional vegetation (Gao et al., 2018a). Successful use of LDA on modern topsoils, and its applicability for paleovegetation reconstructions, have been demonstrated by Gao et al. (2018a). Weighted averaging partial least squares (WAPLS) regression was used to quantitatively reconstruct tree coverage for the study region, using the 'wpls' function in the 'rioja' package of R (Juggins, 2020). Variation partitioning was performed using the 'varpart()' function in the 'vegan' package of R (Oksanen et al., 2020). The tree cover percentage for each modern topsoil site was extracted from a 2000–2012 averaged tree canopy cover dataset (Hansen et al., 2013). All statistical analyses were performed in R 4.0.2 (R Core Team, 2020) with RStudio v 1.3.1073 (RStudio Team, 2020).

2.4. The dynamic vegetation modelling approach

The dynamic vegetation-ecosystem model LPJ-GUESS (Smith et al., 2001, 2014) was used to simulate the regional vegetation cover for the mid-Holocene (MH) and pre-industrial interval (PI). LPJ-GUESS is a state-of-the-art dynamic global vegetation model (DGVM) that can simulate structural, compositional, and functional properties of the global ecosystem of major climate zones, given either observed or modelled climate conditions and atmospheric carbon dioxide concentrations (Smith et al., 2001, 2014). The model with a spatial resolution of $\sim 1^\circ$ of latitude by 1° of longitude was employed in this study. The simulated vegetation dynamics are based on the growth and competition of woody plant individuals and an herbaceous understory in replicate patches within each $1^\circ \times 1^\circ$ grid cell. The representative patches form the dominant plant functional types differing in growth form, phenology, photosynthetic pathway, and bioclimatic limits. The DGVM approach has been shown to perform well reproducing ecosystem transitions in monsoon regions associated with paleoclimate variations, such as those in western Africa (Lu et al., 2018), Amazonia (Kukla et al., 2021), and Australia (Lu et al., 2019). Therefore, this approach could provide a mechanistic perspective on the effects of climate on vegetation change.

In the present study, two contrasting scenarios were simulated to assess the response of vegetation to climate shifts in the East Asian monsoon margin area. For simplicity, the PI forcing simulation was used as the benchmark for the late Holocene, which allowed the CO₂ fertilization effect (e.g., Poorter and Navas, 2003) to be disregarded. Compared with the PI simulation, the MH simulation employed significantly higher temperature and precipitation parameters primarily driven by stronger summer insolation in northeastern Asia in the mid-Holocene. The PI and MH climate forcing variables for LPJ-GUESS were obtained from fully coupled general circulation model (GCM) simulations using EC-Earth (Hazeleger et al., 2010; Pausata et al., 2016). The LPJ-GUESS models began with barren ground, extended for 500 years to reach an equilibrium state, then continued for 20 years.

Additional information about the baseline PI and MH LPJ-GUESS simulations appears in Lu et al. (2018).

Two sensitivity simulations were performed to separately observe the impacts that precipitation and temperature have on East Asian monsoon margin vegetation change. In simulation MH_PI_temp, all climate forcing variables of the MH were used except for temperature; PI temperatures were substituted into the forcing to elucidate the effects of temperature change on vegetation. Similarly, in MH_PI_prec, the precipitation was set at the PI level to investigate the precipitation forcing effects for the MH.

3. Results

3.1. Physical and chemical composition of peat core HSP-2

As shown in Fig. 2, total organic carbon (TOC) content of the top (upper 24 cm; 440 cal. yr BP to present) and bottom (72–84 cm; 5100–4320 cal. yr BP) parts of the core are higher than in the middle parts of the core. The pattern for ash content is the same as that for TOC (Figs. 2 and S1). The humification profile of core HSP-2 is similar to that for TOC, displaying high absorbance, above 20% on average, near the top of the section, decreasing down-core from there, and increasing again to 10–15% at the bottom of the core (Fig. 2). Peat humification correlates positively with TOC (negatively with ash content) at a statistically significant level ($r = 0.854, p < 0.001, n = 68$).

3.2. Grain size distribution and sediment composition

Silt dominates the mineral sediments within the peat, comprising on average more than 65% of the clastic material (Fig. 2). The sand fraction accounts for a lower percentage of mineral sediments in the basal part of the core but increases substantially from a depth of 30 cm to the top of the core. Grain-size distributions for most samples range from 1 to 200 μm , displaying unimodal and multimodal distributions (Fig. 3a). These grain size distributions suggest that clasts in the peat originated from various sources/dynamics. Plotting SD vs. grain size reveals two distinct peaks (Fig. 3b) at 5.5 μm and 296 μm , with graphical troughs at 32–90 μm (Fig. 3b). The grain size classes (C2: 32–90 μm) that have smaller SD values (also known as insensitive components), divide the grain classes into two high SD groups, namely C1 (<32 μm) and C3 (>90 μm). The mineral grain-size abundances of C1 and C3 covary negatively along the HSP-2 peat core at a statistically significant level ($r = -0.959, p < 0.001, n = 71$; Fig. S2).

3.3. Phytolith assemblages and vegetation reconstructions

3.3.1. Frequency, absolute abundance, and influx of phytolith assemblages and their variations through peat core HSP-2

All samples yielded abundant phytolith types attributed to different families of grass and occasionally trees (Plate I). The phytolith assemblage frequency (in percentage) varied slightly throughout the core, and is dominated by ELONGATE ENTIRE, RONDEL, TRAPEZOID, CRENALE, and ACUTE BULBOSUS (Fig. 4a). TRAPEZOID, CRENALE, and RONDEL forms, typical of C3 Pooideae (Twiss et al., 1969; Kondo et al., 1994), represent more than 45% of the observed phytoliths. BILOBATE phytoliths account for about 3% on average among all the samples, whereas the SADDLE types represent no more than 1% on average.

Absolute abundance (Fig. 4b) and phytolith influx (Fig. 4c) displayed notable variations in the core. Interestingly, the absolute phytolith abundance, as well as phytolith influx, correlates with the TOC content of the sample (Fig. S1). CONISS identified several first-order phytolith stratigraphic zones in peat core HSP-2 throughout the 5100-year sequence (Fig. 4a–c). The zones are similar, displaying few differences in relative abundance, absolute abundance, and influx diagrams. The phytolith assemblage can be divided into five different zones (stages).

Zone I (76 to 84 cm; 5100 to 4590 cal. yr BP) is characterized by a

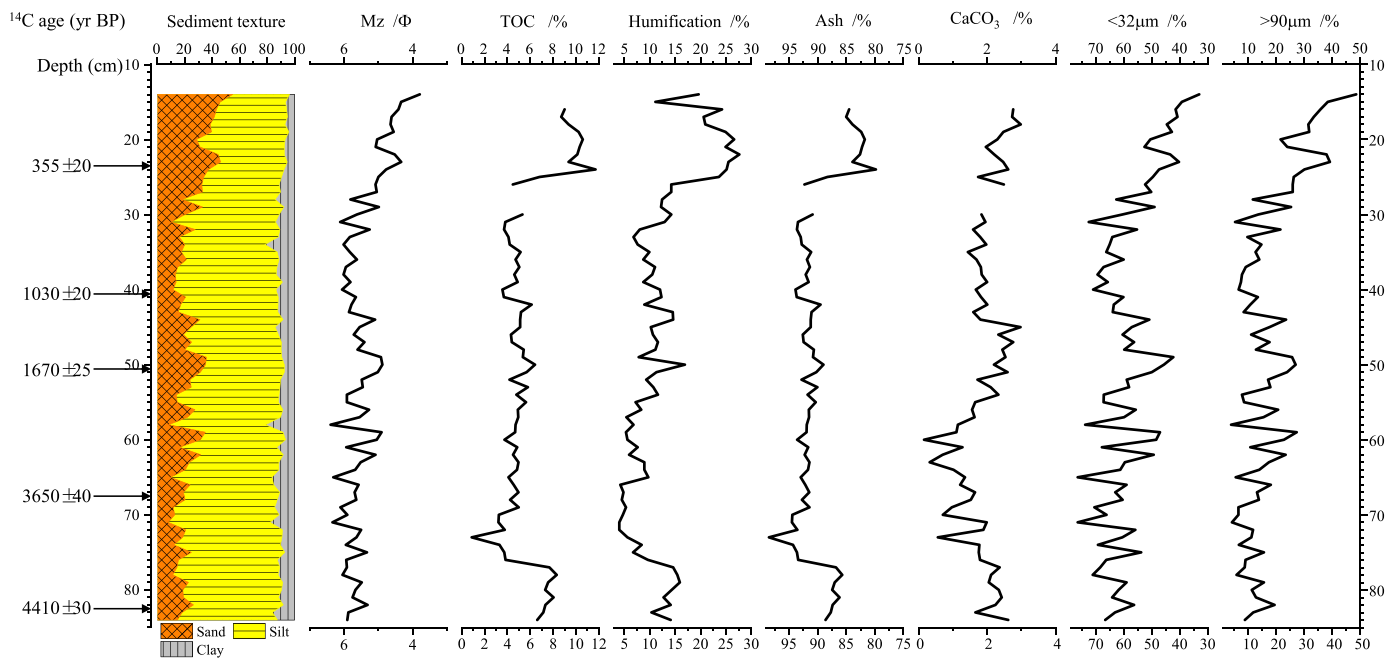


Fig. 2. Textural composition, physical, and geochemical profiles of peat core HSP-2.

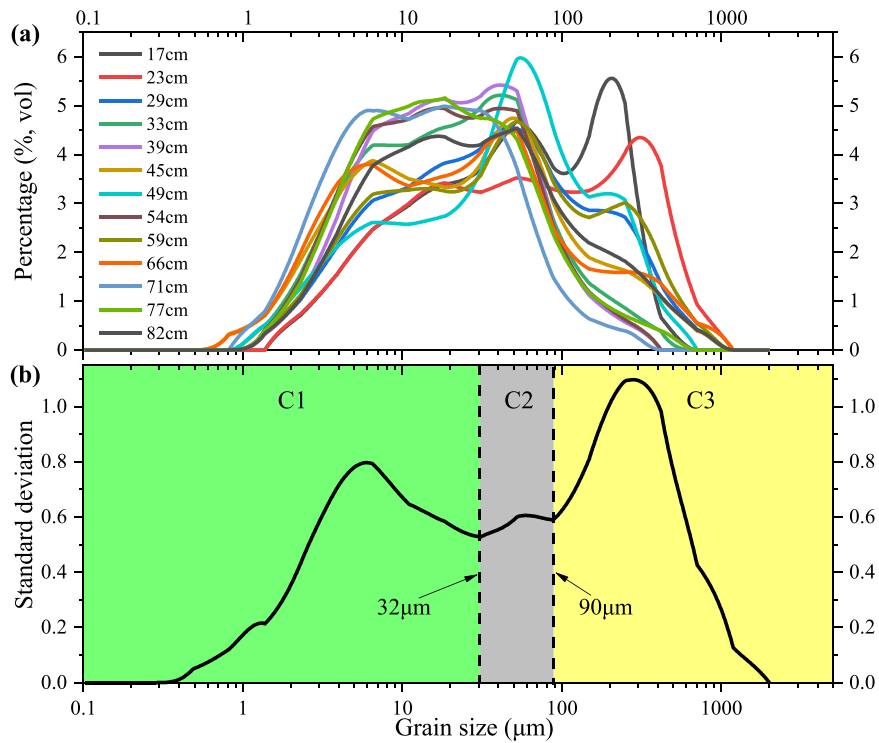


Fig. 3. (a) Grain size frequency distributions of selected peat samples and (b) grain-size classes vs. standard deviation (SD) diagram of HSP-2 peat core.

high phytolith concentration (absolute abundance) and high phytolith influx. The averaged phytolith concentration is 5×10^6 grains/g while the phytolith influx is about 8×10^4 grains/cm²/yr (Fig. 4b and c). Despite CONISS identifying several first-order zones in the dendrogram (Fig. 4a), visual inspection shows very few notable differences between Zone I and adjacent zones, suggesting that only small differences occur in the phytolith frequency diagram (Fig. 4a). ELONGATE ENTIRE, RONDEL, TRAPEZOID, CRENALE, and ACUTE BULBOSUS account for more than 90% of the total assemblage and display significant fluctuations within this stage

(Fig. 4a).

In Zone II (48 to 76 cm; 4590 to 1330 cal. yr BP), a dramatic decrease in absolute phytolith abundance is recorded in the concentration and influx diagrams (Fig. 4b and c). Especially at the interval of 70–75 cm (4520 to 4170 cal. yr BP), the phytolith concentration decreases to 0.6×10^6 grains/g while phytolith influx decreases to 0.8×10^4 grains/cm²/yr (Fig. 4). This event, however, is not visible on the phytolith frequency diagram, where only Cross reaches its highest percentage of the assemblage in the core. Chronologically, this sharp decrease in absolute

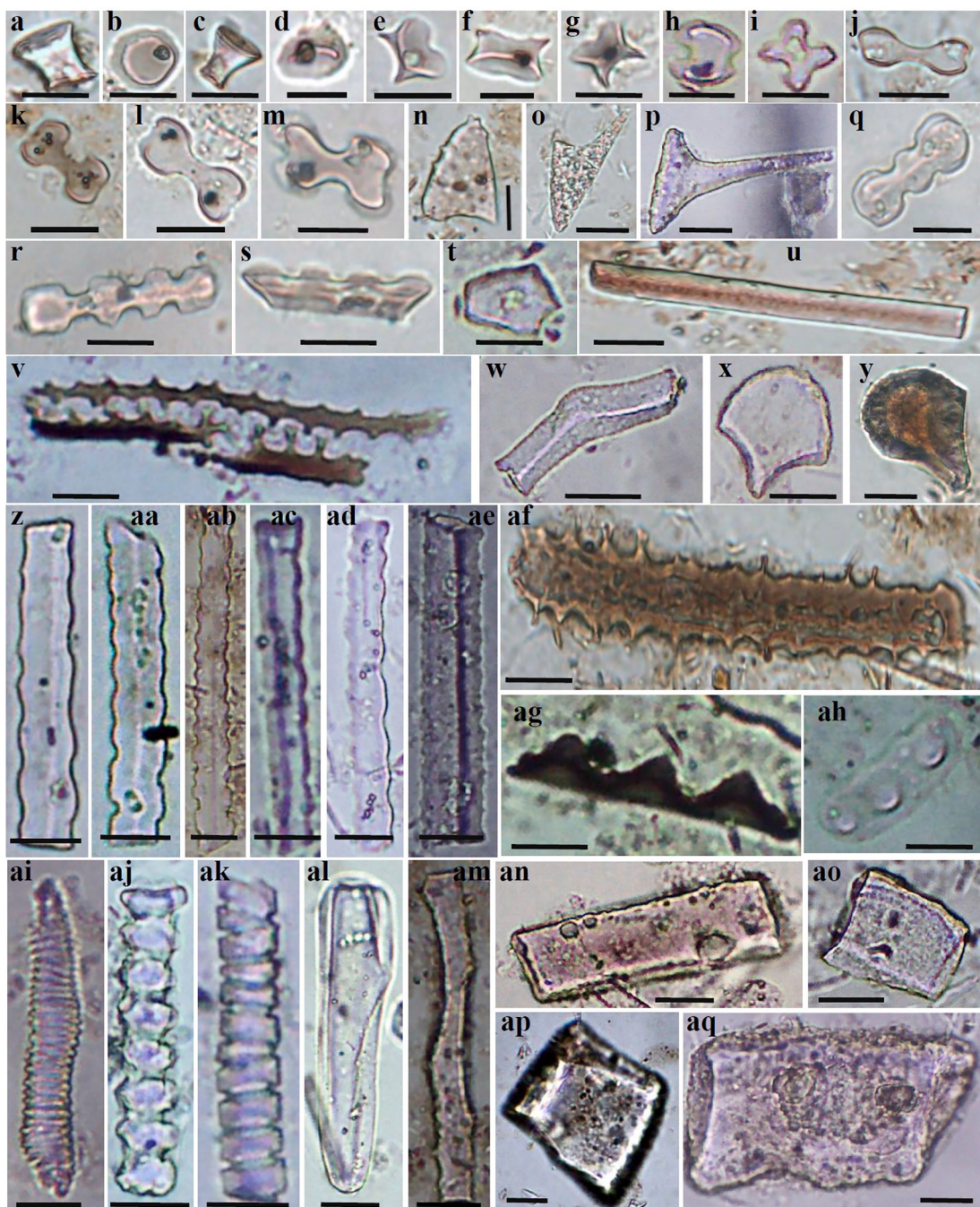


Plate I. Microphotographs of selected phytolith types counted in this study. (a–d) RONDEL; (e–h) SADDLE; (i) CROSS; (j–m) BILOBATE; (n–p) ACUTE BULBOSUS; (q–s) CRENALE; (t) PAPILLATE POLYGONAL; (u) ELONGATE ENTIRE; (v) ELONGATE DENDRITIC; (w) ELONGATE GENICULATE; (x–y) BULLIFORM FLABELLATE; (z–ae) ELONGATE SINUATE; (af) ELONGATE DENTATE; (ag–ah) PAPILLATE; (ai–ak) TRACHEARY ANNULATE/HELICAL; (al–am) ELONGATE ENTIRE; (an–aq) BLOCKY.

phytolith abundance might correspond to the well-known “4.2-ka event.” After 4200 cal. yr BP, the phytolith concentration increased to approximately 3×10^6 grains/g and fluctuated around the average level (3×10^6 grains/g) of Zone II.

Zone III (42 to 48 cm; 1330 to 1000 cal. yr BP) is characterized by an “event-like” increase in absolute phytolith abundances (Fig. 4). Compared to Zone II, the phytolith concentration (influx) increases dramatically to 14.5×10^6 grains/g (Table S3), which is about five times higher than the average value of Zone II. After the sharp increase in phytolith concentration (influx), the absolute phytolith abundance fluctuated significantly, but the average abundance is still higher (phytolith concentration is 6.4×10^6 grains/g, and phytolith influx is 12

$\times 10^4$ grains/cm 2 /yr) than in Zone II.

Zone IV (30 to 42 cm; 1000 to 600 cal. yr BP) is another period with significantly lower absolute phytolith abundances, despite phytolith frequency showing imperceptible variation. The mean phytolith concentration declined to 1.6×10^6 grains/g (phytolith influx decreased to 4.9×10^4 grains/cm 2 /yr) during this stage.

In Zone V (14 to 30 cm; 600 to 240 cal. yr BP), the phytolith assemblage indicates significant vegetation and sedimentary environmental succession at the coring site. The phytolith assemblage is dominated by various ELONGATE types (such as ELONGATE ENTIRE, ELONGATE DENTATE). ACUTE BULBOSUS, BILOBATE. Meanwhile, the average percentage of CROSS types were the highest of the core (Fig. 4a), NON-HERB phytoliths,

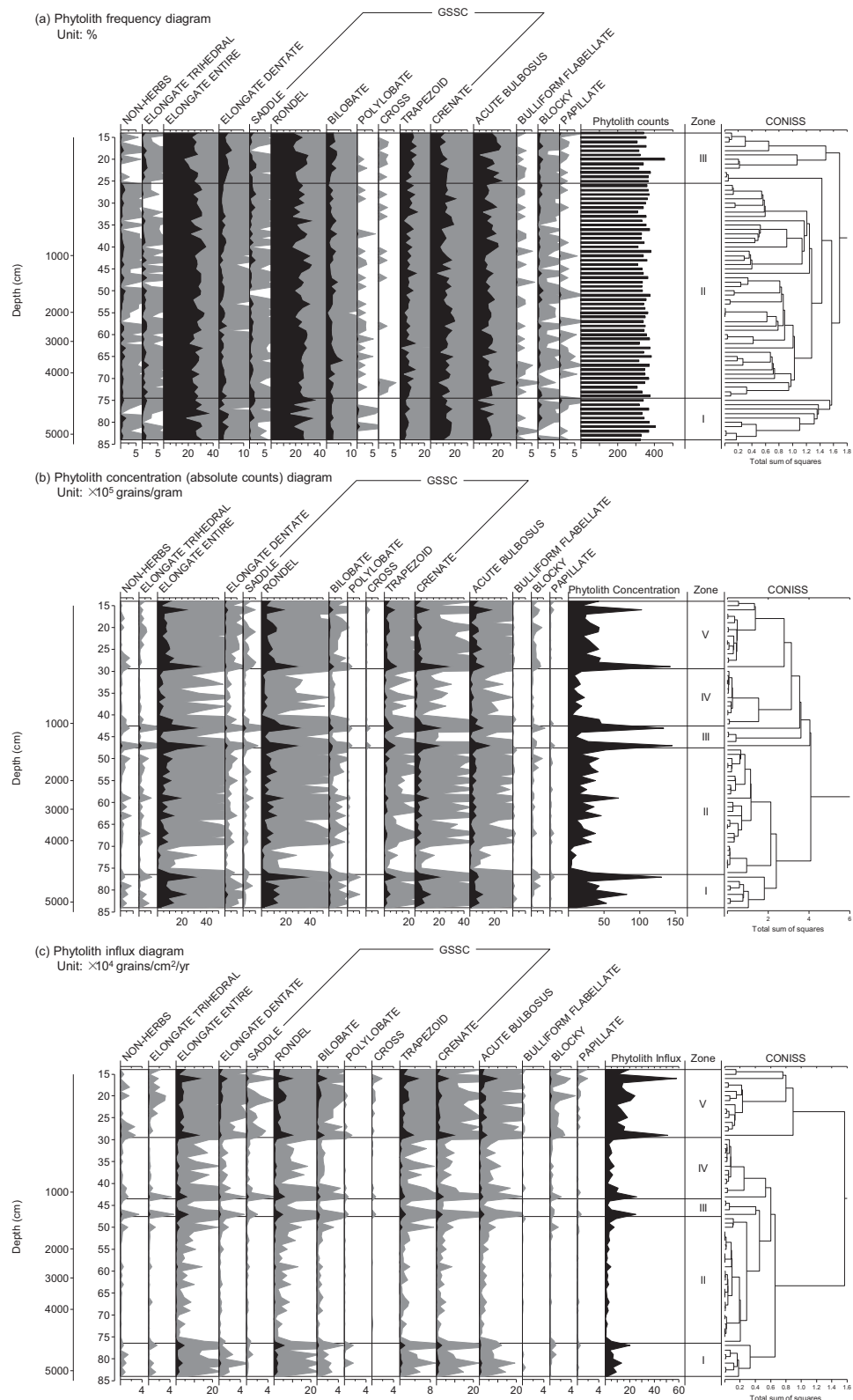


Fig. 4. Relative and absolute abundance of phytoliths (selected categories) observed in peat core HSP-2. Exaggeration ($\times 10$) is indicated by grey shading. (a) Phytolith frequency diagram; (b) Phytolith concentration diagram; (c) Phytolith influx diagram.

however, are at their lowest values in the core, suggesting a change in the local peatland and surrounding vegetation. Interestingly, the absolute phytolith abundance increases again (4.5×10^6 grains/g on average) and phytolith influx reaches its highest values (20.3×10^4 grains/ cm^2/yr) in the entire core. The high absolute phytolith

abundance stage (Zone V) corresponds to the high TOC and humification degree at the top section of core HSP-2 (Fig. 2). Phytolith (Fig. 4) and geochemical composition (Fig. 2) evidence suggest that the coring site may have evolved into a typical wetland environment with local wetland species contributing to the fossil phytolith assemblage by that

Table 2

Performance of WAPLS model relating to canopy tree coverage and phytolith variance.

Model	Apparent			Cross validation		
	RMSE (%)	R ²	Max bias (%)	RMSE (%)	R ²	Max bias (%)
WAPLS-1	17.3217	0.259	44.2434	18.1132	0.1933	46.9288
WAPLS-2	15.6565	0.3946	39.0265	17.8371	0.2378	45.4867
WAPLS-3	14.6289	0.4715	35.5493	18.2844	0.2256	45.8895
WAPLS-4	14.1141	0.508	32.6258	18.5059	0.2293	45.1269
WAPLS-5	13.8464	0.5265	30.7388	18.9136	0.2126	43.9372

time.

3.3.2. Phytolith-based vegetation composition and tree coverage reconstructions

Employing WAPLS regression, the phytolith-based modern canopy tree coverage estimates match satellite data well (Hansen et al., 2013). Table 2 lists the performance of transfer functions established to reconstruct past canopy coverage surrounding the Hongshuipao peatland. The five-component WAPLS model has the most robust performance statistics (Table 2 and Fig. 5), with satisfactory estimates of percent variance explained and root mean squared error (RMSE) for tree coverage ($R^2 = 0.527$, RMSE = 13.846) (Fig. 5). Application of the phytolith-based tree coverage inference model to the peat core indicates that the tree coverage surrounding the peatland generally declined during the past five millennia (Fig. 6) with the reconstructed tree cover ranging from 10% to 40%.

Discriminant analysis results indicate the occurrence of predominantly forested communities surrounding the investigated peatland. Using four linear discriminant functions established by the modern topsoil phytolith assemblages, each fossil phytolith assemblage from peat core HSP-2 was assigned to a specific vegetation category—*Larix*-mixed forest, *Pinus*-mixed forest, broadleaf forest, grassland, and open woodland forest (Gao et al., 2018a). The phytolith-based paleo-vegetation reconstruction demonstrates that the study region has experienced vegetation succession since 5100 cal. yr BP (Fig. 6). The probabilities of *Larix*-mixed forest and *Pinus*-mixed forest covaried

negatively throughout the profile and the sum of their likelihoods on average account for more than 93.50%, suggesting that they have likely been the dominant communities for the study area in the past five millennia. In general, the probability of a *Larix*-mixed forest increased from the bottom to the top of the core. It peaked at 4500–4000, 3000–2500, 2000–1500, 1000–300 cal. yr BP, during which the probability of a *Pinus*-mixed forest decreased. The probability of a broadleaf forest increased during the two intervals of 4900–4300 cal. yr BP and 3400–1500 cal. yr BP. Grassland likelihood is much lower than that of forest, and occurs at 4700–4000 cal. yr BP and ca. 400–300 cal. yr BP (Fig. 6). Phytolith assemblages in the Hongshuipao peatland rarely represent typical grassland, suggesting that forest cover persisted in the study region since the mid-Holocene (Fig. 6).

3.4. Holocene tree pollen synthesis for the monsoon margin area

Tree pollen percentage has been used as a proxy for paleoclimate and landscape openness (e.g., Chen et al., 2015; Cui et al., 2019). Synthesis (z-scores) of 11 published lacustrine pollen records shows a general shift in vegetation that approximately coincided with variations of EASM intensity (e.g., Dong et al., 2010). Tree pollen percentages in most cores were lower during early Holocene but started to increase after ca. 7800 cal. yr BP (Fig. S3). Stacked tree pollen z-scores reached maximum values during the mid-Holocene (7800–4000 cal. yr BP). After 4000 cal. yr BP, tree pollen z-scores gradually decreased and reached their lowest values in the last millennium (Fig. S3). This significant decrease of tree pollen from the middle to the late Holocene implies that the monsoon margin vegetation succession may have been caused by climate shifts in East Asia (see discussion section). Some discrepancies, however, exist among different records. Especially during the interval from approximately 4000 to 1000 cal. yr BP, the stack uncertainties (as reflected by standard deviations of the 11 records in Fig. S3) increase to peak values from 2000 to 1000 cal. yr BP, implying that site-specific differences might become more important during that period.

3.5. Variation partitioning analyses and LPJ-GUESS simulations

Variation partitioning analyses indicate that climate alone explained the highest fraction of variation (15%) in phytolith-estimated vegetation composition and tree cover during the entire period under investigation (Fig. 7a). The variation explained by human population size and forest fires, moreover, is relatively low (Fig. 7a). Results of the moving window approach demonstrate the strong impact of climate on vegetation

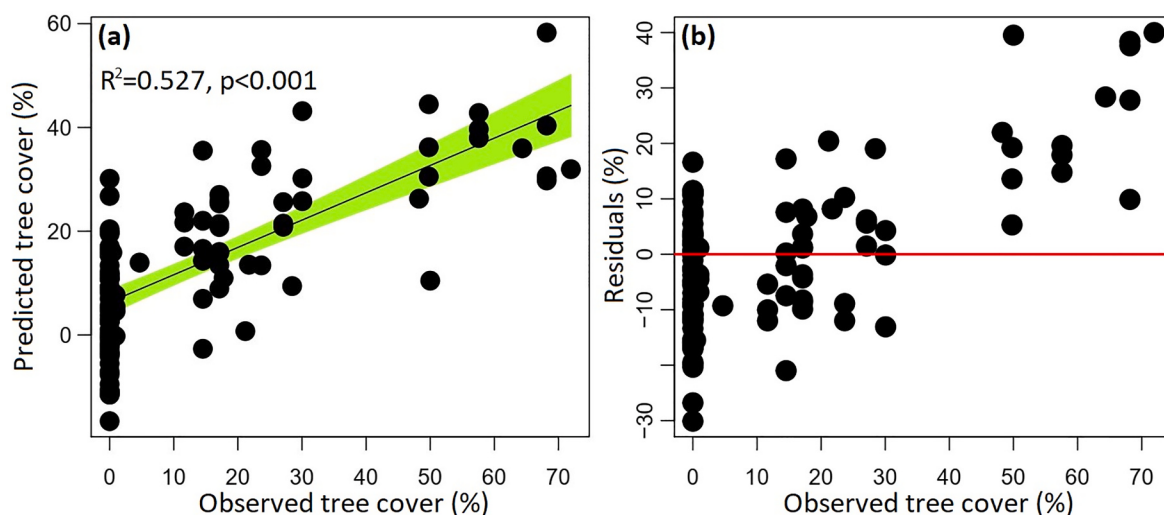


Fig. 5. The 5-component WAPLS inference model results for (a) the observed versus inferred tree coverage (%), and (b) the observed tree coverage versus residual values.

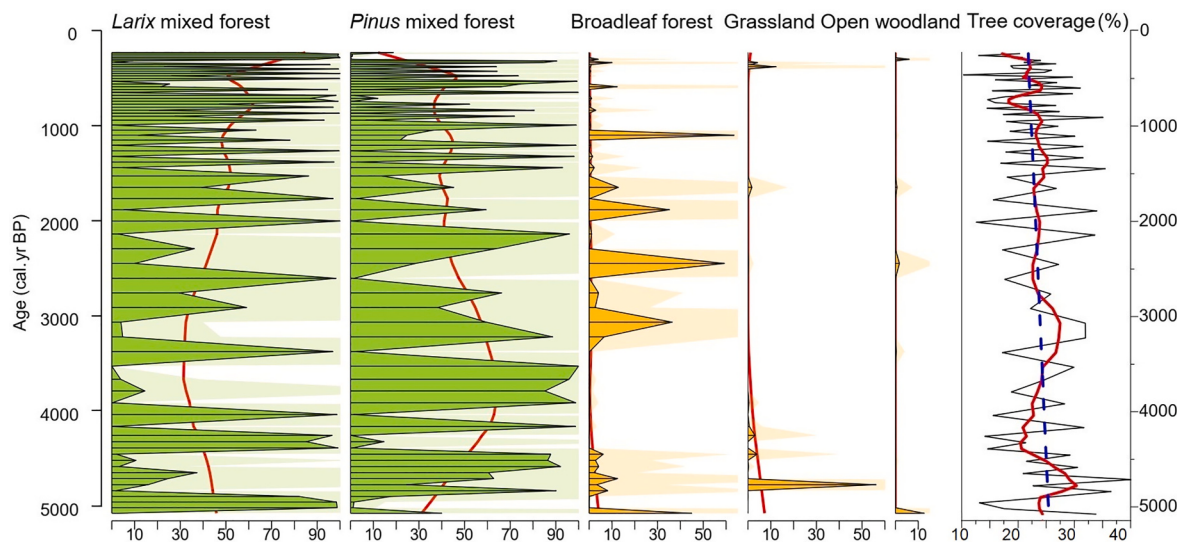


Fig. 6. Discrimination probability of different vegetation composition and WAPLS reconstructed canopy coverage using fossil phytolith assemblages from core HSP-2. The colored shades denote the exaggeration (x5).

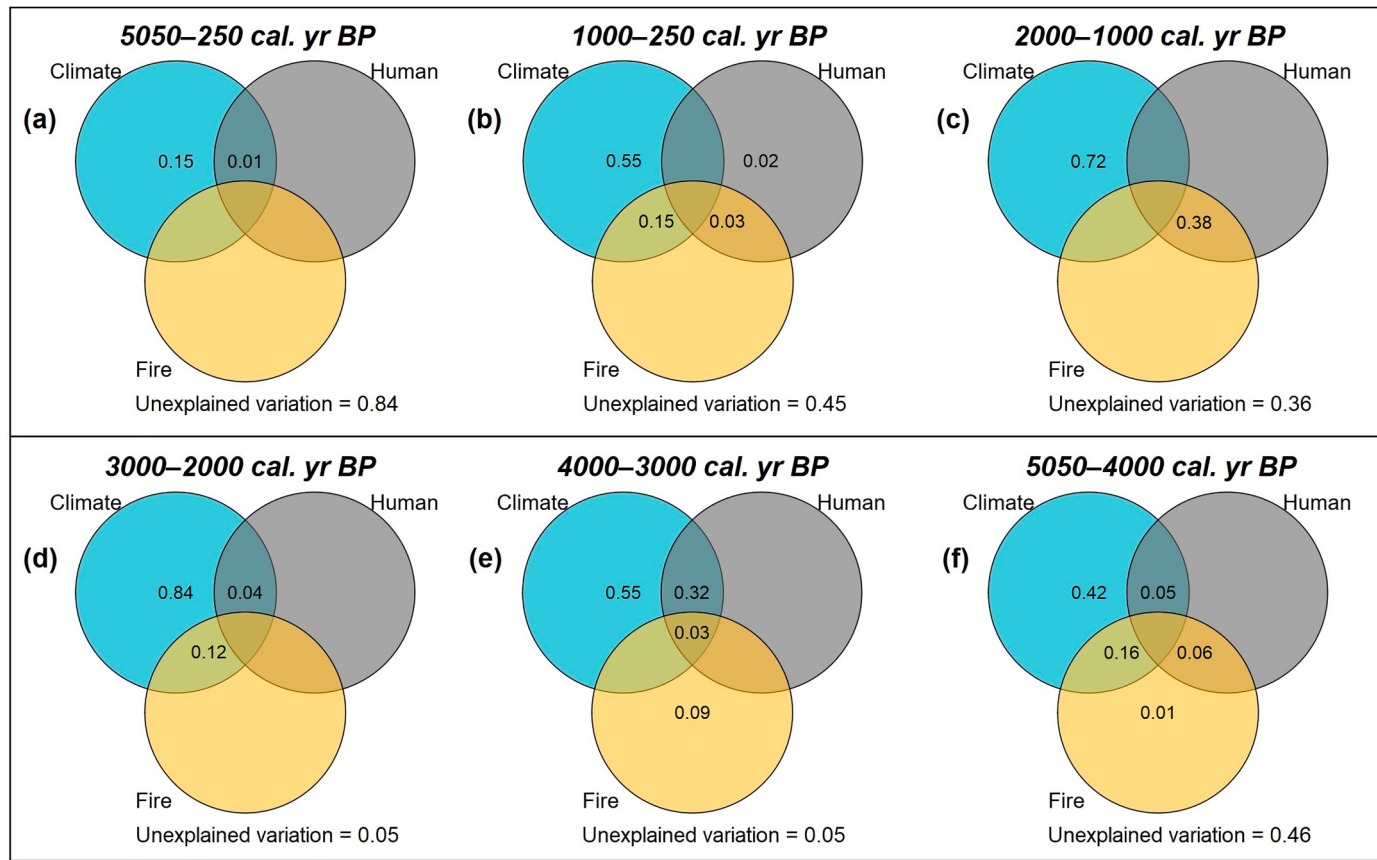


Fig. 7. Variation in vegetation composition explained by climate, human population, and fires during (a) the whole study period (5050–250 cal. yr BP), (b) 1000–250 cal. yr BP, (c) 2000–1000 cal. yr BP, (d) 3000–2000 cal. yr BP, (e) 4000–3000 cal. yr BP, and (f) 5050–4000 cal. yr BP. Values <0 are not shown in the figure.

dynamics from the middle to the late Holocene (Fig. 7b–f), ranging from 42 to 84%. The relative importance of climate was slightly lower during 5050–3000 cal. yr BP, when fire's importance was generally higher and explained about 9% of the variation in vegetation (Fig. 7e and f). However, because paleofire frequencies during 5000–3000 cal. yr BP were significantly lower than during the last two millennia (Xu et al.,

2021), the relatively high explanatory values of paleofire might be linked to long-term climate change (Xu et al., 2021). The importance of human population size increased at approximately 2000 cal. yr BP, explaining up to 2–5% of the variation in vegetation change (Fig. 7b and c) and indicating that human impacts on landscape composition intensified over the last few millennia.

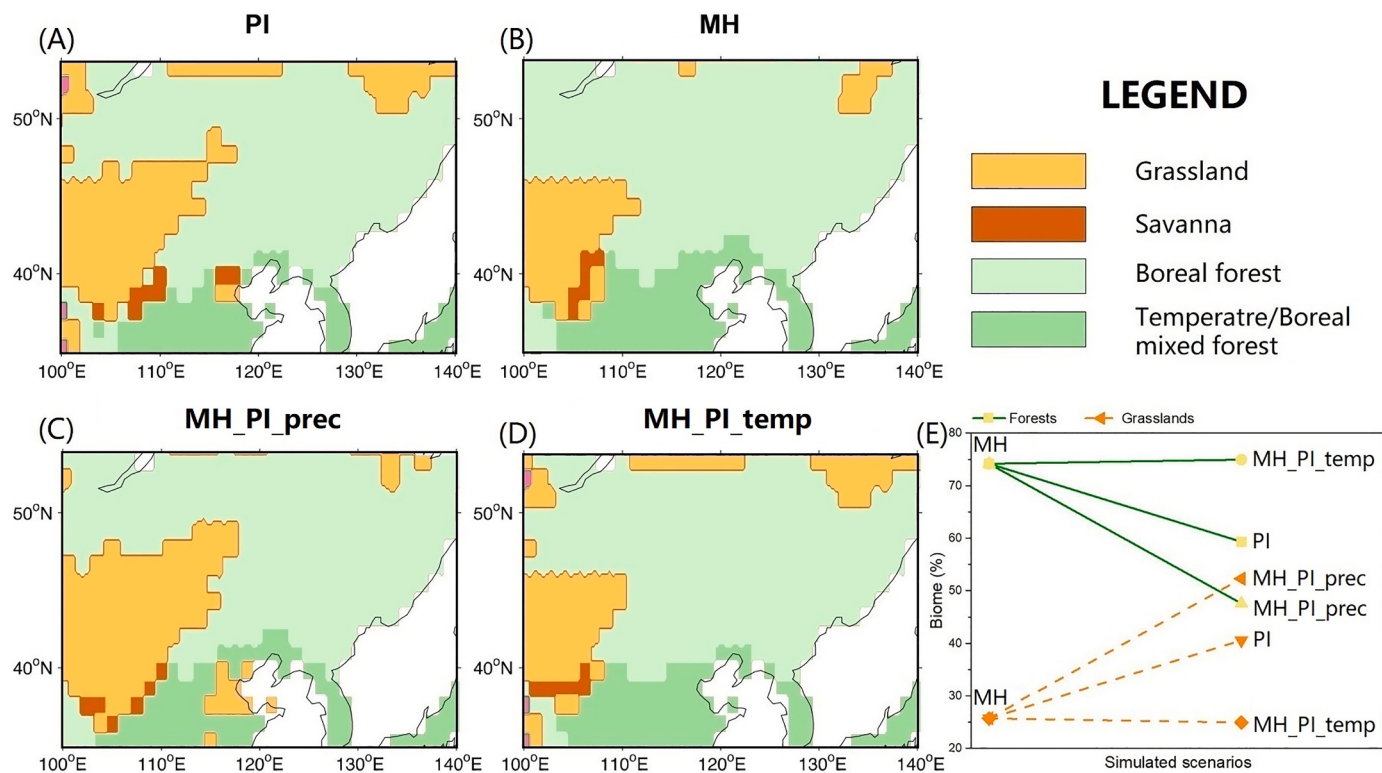


Fig. 8. Maps of dominant vegetation types (LPJ-GUESS simulated) and their abundances for the study region under different scenarios. (A) PI; (B) MH; (C) MH_PI_prec: MH but with PI precipitation; (D) MH_PI_temp: MH but with PI temperature; (E) forest and grassland biome fractions for the region of interest (40–50°N, 100–120°E). PI denotes preindustrial period; MH denotes mid-Holocene with ‘green Sahara’ vegetation and reduced dust concentration (Lu et al., 2018). (For interpretation of the references to colour in this figure legend, the reader is referred to the web version of this article.)

Considering the low explanatory values of paleofire and human population, it is reasonable to employ dynamic global vegetation models (DGVM: LPJ-GUESS) to evaluate the response of vegetation composition and distribution to temperature and precipitation change. In LPJ-GUESS simulations, the forest-grassland boundary during the MH was at approximately 45°N (Fig. 8B) mainly due to forest-favorable climate. However, due to comparatively low air temperature, soil temperature, and precipitation in the PI stage (Fig. S4), grasslands extended from northern China to ~50°N (Fig. 8A). These trends are also reflected in the modelled relative abundance values of forest and grassland (Figs. 8E and S5); the abundance of forest decreased from 74.22% (MH) to 59.37% (PI) while that of grassland increased from 25.78% (MH) to 40.63% (PI).

Sensitivity experiments suggest that precipitation is the main factor that has been driving the vegetation shift since the mid-Holocene. When the PI temperature is prescribed, the simulated forest fraction remains almost the same under the MH (74.22%, Fig. 8B) and MH_PI_temp (75%) scenarios (Figs. 8D and E and S5). This forest fraction, however, is quite sensitive to precipitation changes, decreasing to 47.65% when the precipitation is set to the PI level, namely under the MH_PI_prec scenario (Fig. 8C and E). These results suggest that the distribution and variation of forest/steppe coverage are sensitive to precipitation rather than temperature changes.

4. Discussion

4.1. Reliability of phytolith-based paleovegetation reconstruction and its comparison with the pollen-inferred landscape

4.1.1. Phytolith source, taphonomy, and representative biases

Phytoliths are generally deposited in place. A phytolith assemblage extracted from a topsoil sample likely represents the long-term standing

vegetation growing at the sampling location. However, fossil phytoliths preserved in lacustrine or peaty sediments are not directly comparable to topsoil phytoliths since there are various taphonomic processes affecting the interpretation of sedimentary records. These processes correspond to bias associated with the production, transport, deposition, and conservation of phytoliths in a sedimentary archive (cf. Aleman et al., 2014).

Production differences of phytolith morphotypes can introduce significant bias in paleovegetation reconstruction by over- or under-representing some of them. In this study, WAPLS and discrimination analysis indicate that *Larix*-mixed forest and *Pinus*-mixed forest are the most likely dominant communities for the study area (Fig. 6). However, the phytolith assemblage in peat core HSP-2 was dominated by grass silica short-cell phytoliths (GSSCP) with an average abundance of >50% (Fig. 4a), showing strong over-representativeness to Poaceae species. At the same time, arboreal phytoliths make up less than 2% of the phytoliths on average throughout the peat section (Fig. 4a), indicating strong under-representativeness to trees.

Besides production differences, phytolith source and transport factors may also affect a phytolith assemblage. Phytolith assemblages in a lake-transformed peatland is probably not representative of the vegetation surrounding the peatland basin because wetland species growing directly on the peat should provide most of the phytolith input. The Hongshuiapao peatland is slightly different from a typical lake-transformed peatland: it was developed in the broad valley of the Tuoxin River (Fig. 1C) and may at times be subject to fluvial influences. This geomorphological and sedimentary setting could have caused the coring site to receive more regional phytoliths than would a closed peatland, which is characterized by a small catchment area and composed exclusively of macrofossils (higher TOC contents but lower ash contents). Fluvial sediments constitute a large portion of the investigated sediments, as reflected by the relative low TOC contents (<6%

on average) and higher ash contents (>90%) (Fig. 2). Phytoliths produced by the regional vegetation would likely be transported to the peatland by surface runoff. Nevertheless, the percentage of extra-local phytoliths cannot be estimated accurately. Thus, it is assumed that at least some of the phytoliths are associated with relative long-distance

dispersal and could record at least part of the regional vegetation information. Our phytolith-based vegetation reconstruction is of regional importance rather than a site-specific local signal.

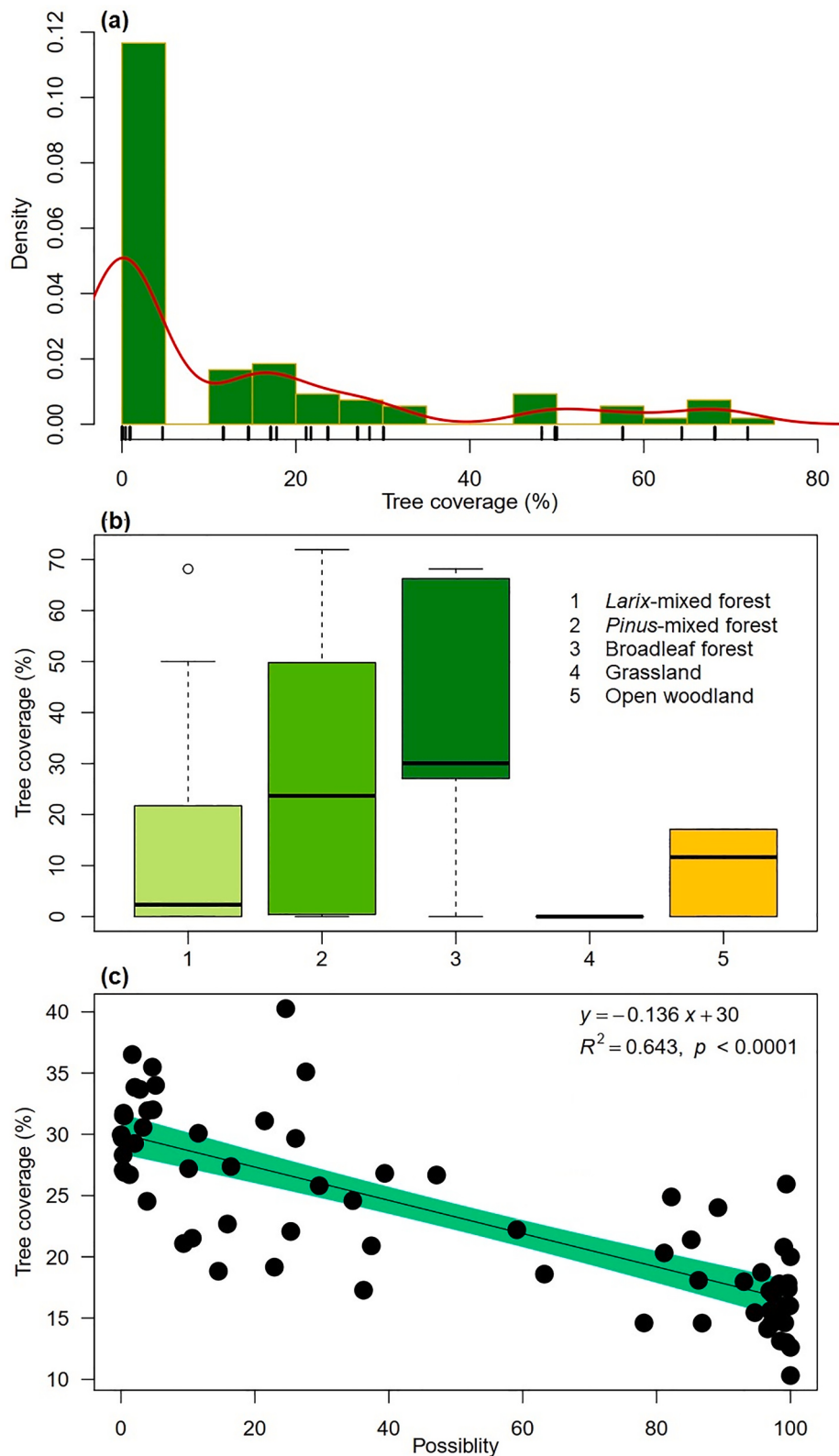


Fig. 9. (a) Tree coverage-frequency histogram of the modern training phytolith dataset. (b) Box plots of tree coverages under different vegetation types in modern training set. (c) Correlation between WAPLS reconstructed tree coverage and the probability of *Larix*-mixed forest.

4.1.2. Limitations and implications of topsoil phytolith-based quantitative tree coverage estimation

As shown in Table 2, although the five-component WAPLS model predicted tree coverage closely approximating the satellite imagery observations (Fig. 5), the leave-one-out cross-validation suggests that the five-component WAPLS model does not have a strong coefficient of determination ($R^2 = 0.213$) nor a lowered root mean square error of prediction ($\text{RMSE} = 18.914\%$). Several factors may account for this low accuracy of tree coverage reconstruction. First are weaknesses in the modern training dataset. When establishing a WAPLS regression, Turner et al. (2021) claimed that the sampling range and continuity of modern reference sites are more important than the number of samples. Although the modern topsoil reference set spanned the five different vegetation types across northeastern China, the canopy coverage for those sites varied significantly. For instance, non-forest quadrats (tree cover = 0%) account for more than half of the total modern topsoil samples (Fig. 9a). Second, the modern training set lacks samples in some of the canopy coverage intervals – 5–10%, 35–45%, and > 80%, and this also increases the prediction uncertainties of the transfer function (Turner et al., 2021). A third possible reason for low accuracy might derive from the multiplicity and redundancy nature of phytoliths (Piperno, 1988; Barboni and Bremond, 2009). One principal assumption of WAPLS is that taxa used for reconstruction show a unimodal response to the climate variable being reconstructed. For phytoliths, however, this could be complicated because a given taxon produces multiple phytolith types (multiplicity), and a given phytolith shape may be produced by many taxa (redundancy) (Piperno, 1988; Barboni and Bremond, 2009). These factors might have impeded the establishment of a highly accurate tree coverage transfer function, which would result in less stable model performance during cross-validation.

Despite the above caveats, the topsoil phytolith-based canopy coverage reconstruction correlated negatively with the discriminant probability of *Larix*-mixed forest ($R^2 = 0.643, p < 0.001, n = 71$, Fig. 9c) and positively with *Pinus*-mixed forest ($R^2 = 0.530, p < 0.001, n = 71$) at statistically significant levels. Because quadrats with *Larix*-mixed forest have sparser (lower) canopy coverage than those from *Pinus*-mixed forest (Fig. 9b), and because two independent methods (WAPLS and LDA) were used separately, the consistency between the canopy coverage reconstructions and linear discrimination results (Fig. 6) indicates that phytolith analysis can reproduce canopy coverage with sufficient success from fossil phytolith data, especially when comparing variation trends.

4.1.3. Comparisons between pollen- and phytolith-reconstructed landscape and tree coverages

Using the modern phytolith training set and discriminant analysis, our reconstructions suggest that regional vegetation surrounding the Hongshupao peatland has primarily been forest with grassland appearing infrequently (Fig. 6). This result differs from pollen reconstructions, which have suggested a forest-steppe landscape (e.g., Wu et al., 2019). Moreover, within the phytolith-identified forest, the dominant (constructive) species varied over time in possible association with climate change (Fig. 6).

Because of the production, dispersal, and over-representative character of *Pinus*, *Betula*, *Artemisia*, and *Chenopodiaceae* pollen in arid and semiarid lands, detailing vegetation composition and evolution from pollen is problematic. Palynologists often use proxies, such as A/C (*Artemisia* to *Chenopodiaceae* ratio), A/Cy (*Artemisia*/Cyperaceae), and AP/NAP (arboreal/non-arboreal pollen ratio), to reconstruct vegetation-associated climate change in these regions (e.g., Liu et al., 2002, 2010; Hao et al., 2014; Cui et al., 2019), and coexistence of arboreal and herbaceous pollen have been interpreted as coexistence of tree and grassland ecosystems, namely forest-steppe. Investigations of modern pollen-vegetation relationships in the study area, however, do not support the validity of that interpretation (Cui et al., 2019).

Modern vegetation in the central part of the Greater Hinggan

Mountains belongs to the temperate *Larix*-broadleaf mixed forest zone (Qian et al., 2003). The canopy layer is dominated by *Larix gmelinii*, but with some presence of *B. platyphylla*, *Picea* spp., *Q. mongolica*, and other woody species. This community structure is spatially less dense than the broadleaf forest, resulting in abundant herbaceous species in the ground layer (Qian et al., 2003). Investigations of the pollen-vegetation relationship in *Larix*-broadleaf mixed forests have suggested that their pollen assemblages are characterized by a high proportion of tree pollen dominated by *Betula* (>40%) along with *Alnus*, *Larix*, and *Pinus*, whereas pollen diagrams for typical steppes are dominated by herbaceous pollen (>80%) with a predominance of *Artemisia* and *Chenopodiaceae* (cf. Cui et al., 2019). In nearby lacustrine sediments (Lake Moon), tree pollen accounts for more than 40% (on average) of the identified pollen grains, with most of the tree pollen consisting of *Betula* pollen (Wu et al., 2019). Taking into account nearby lake sedimentary pollen assemblages (Wu et al., 2019) as well as results from modern pollen-vegetation studies (Cui et al., 2019), our phytolith-based reconstruction suggests that for the past five millennia the regional vegetation has been similar to that of the present landscape, which alternates between *Larix*-dominant forest and *Pinus*-dominant forest, with the tree cover ranging from 10% to 40% (Fig. 6). With respect to the ground layer, however, the phytolith and pollen evidence both indicate that herbaceous species have not changed much during the past 5100 cal. yr BP. The phytolith assemblage of the peat core is dominated by ELONGATE ENTIRE, RONDEL, TRAPEZOID, CRENEATE, and ACUTE BULBOSUS morphotypes and shows very few visible fluctuations (Fig. 4a). The lacustrine pollen record, moreover, shows a strong dominance of *Artemisia* and *Chenopodiaceae* pollen (Wu et al., 2019), reflecting that the constructive (dominant) species in the herbaceous layer experiences little change.

Despite the discrepancies in production, representativeness, and taxonomic resolution between pollen and phytolith, our phytolith-based canopy coverage reconstruction, tree pollen stack, Non-HERB phytolith percentages, and composited stalagmite $\delta^{18}\text{O}$ records (Zhao et al., 2021) show similar variation trends (Fig. 10). Pearson correlation suggests that the phytolith-estimated tree coverage weakly correlates with the Non-HERB phytolith percentage ($r = 0.205, p = 0.09, n = 71$) and stacked tree pollen z-scores ($r = 0.213, p = 0.003, n = 195$). On the other hand, no correlation was found between the composited stalagmite $\delta^{18}\text{O}$ from northeastern China (Zhao et al., 2021) and phytolith-estimated tree cover (or Non-HERB phytoliths percentage) (Fig. 10). Cross-correlation, however, indicates that these two variables are weakly associated ($r = -0.276, h = 450$ years) when a time lag of 400–450 years is considered (Fig. S6), suggesting that monsoon margin tree coverage is possibly modulated by climate change. Three stages of extensive tree cover, namely 5100–4400, 3500–2500, and 1600–500 cal. yr BP (marked as stages I, II, and III, respectively, in Fig. 10), are identified by the Non-HERB phytolith percentage and tree cover profiles. During each stage, composited stalagmite $\delta^{18}\text{O}$ signals are more depleted in ^{18}O (Zhao et al., 2021), suggesting that canopy coverage in the central Greater Hinggan Mountains is linked to strong East Asian monsoon intensity (Fig. 10). Apparently, during an intensified EASM scenario, increased precipitation facilitates the growth of woody species and eventually results in dense canopy coverage (Woodward et al., 2004; Pan et al., 2013). When the EASM weakens, the water deficit enables herbaceous species with lower water needs to expand in the study region and tree coverage to decrease (Pan et al., 2013).

Comparison of the pollen and phytolith reconstructions underscores that, although poor pollen preservation and the over-representation characteristics of *Artemisia* and *Chenopodiaceae* leave pollen-based paleovegetation composition reconstructions in arid and semiarid lands questionable, the general consistency found here between the phytolith-estimated tree coverage and the tree pollen z-scores indicates that fossil tree pollen percentages could still serve as a good proxy for past canopy coverage estimates.

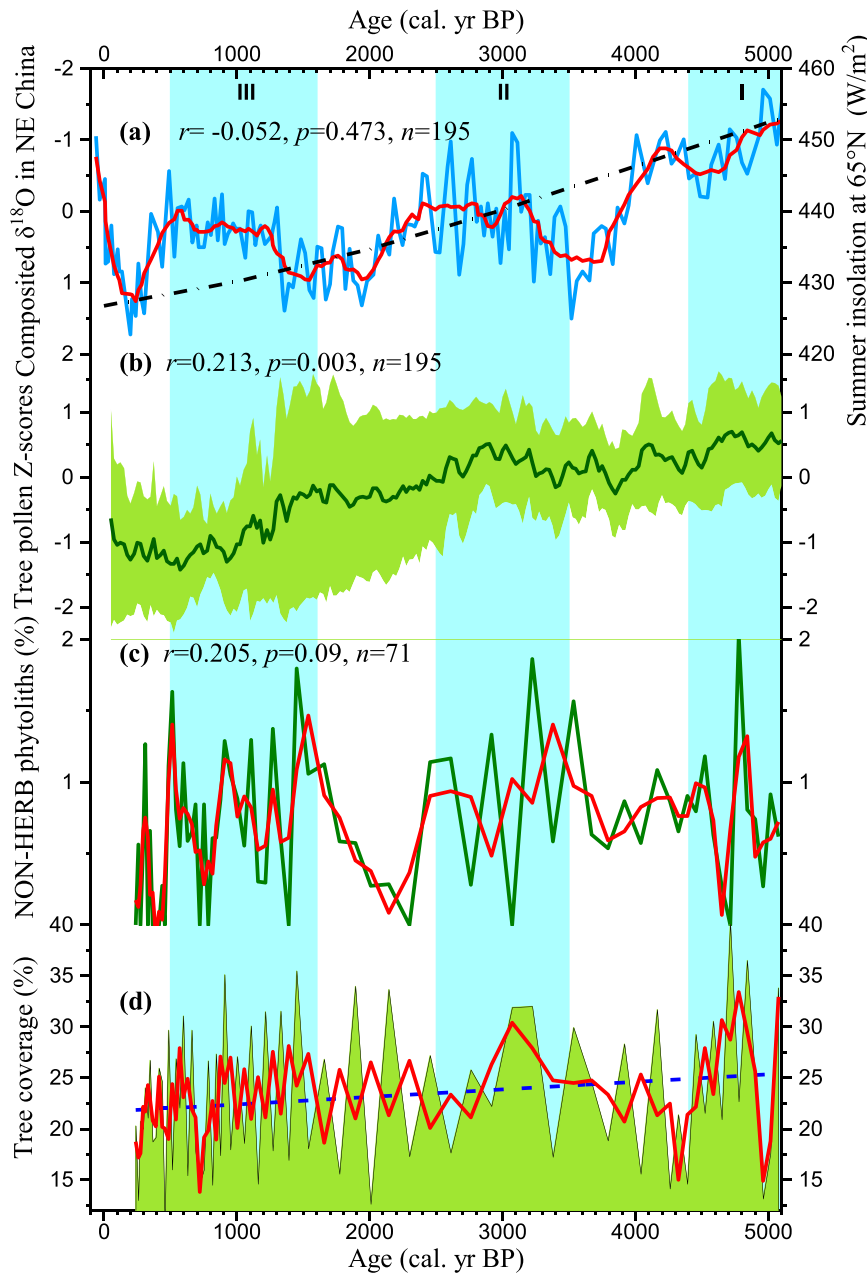


Fig. 10. Phytolith-based tree coverage reconstruction (d) and its comparison with (a) composited stalagmite $\delta^{18}\text{O}$ scores in northeastern Asia (Zhao et al., 2021), summer insolation at 65°N (Berger and Loutre, 1991), (b) stacked tree pollen z-scores along the East Asian monsoon margin (this study), and (c) percentage of Non-HERB phytoliths in core HSP-2 (this study). The Pearson correlation coefficients denote the correlation results between the reference profile (a, b, and c, respectively) and the phytolith-estimated canopy coverage (d).

4.2. Response of vegetation succession to climate change in the northern monsoon margin area

4.2.1. Paleoclimate implications of physical and chemical proxies from the Hongshuipao peatland

(1) Climatic significance of carbonate content and grain-size fractions

Plotting standard deviation vs. grain size class (Fig. 3) identifies two sensitive components (C1 and C3) and one insensitive component (C2). C1 and C3 percentages correlate negatively with each other ($r = -0.959, p < 0.001, n = 71$). Interestingly, C1 shows a weak negative correlation with the carbonate content along the core HSP-2 ($r = -0.396, p < 0.001, n = 68$, Fig. S7), implying a climatic linkage between the fine-grained fractions and carbonate content (Fig. S7).

Although the geochemistry of calcite in a peatland has rarely been investigated (Shotyk, 1988), it may be similar to calcite in lacustrine settings (Fan et al., 2019). Lacustrine calcites in drainage basins without

carbonate rocks are commonly authigenic and directly and/or indirectly related to changes in the lake environment (e.g., Jones and Bowser, 1978; Fan et al., 2019). The Hongshuipao peatland lies in a region of igneous rocks that lacks carbonate rocks. In such settings, dissolution and precipitation of carbonates within peats are regulated by the peatland hydrology, which is directly influenced by the regional climate: carbonates would precipitate first during a drier interval (Shotyk, 1988; Fan et al., 2019). The negative correlation between the fine-grained component and carbonate content may be because more fine clasts are present in the peatland during wet intervals (lower carbonate content).

Various processes can impact sediment particle size, including source rock composition, chemical weathering, hydrodynamic sorting, and alteration after deposition (Hatano et al., 2019). Considering the regional climate information derived from other proxies (e.g., carbonate content) and diatom-based water-table reconstructions (Li et al., 2020a) from peat core HSP-2 (Fig. 11), C1 is most likely associated with chemical weathering regulated by regional climate change (Fig. S7).

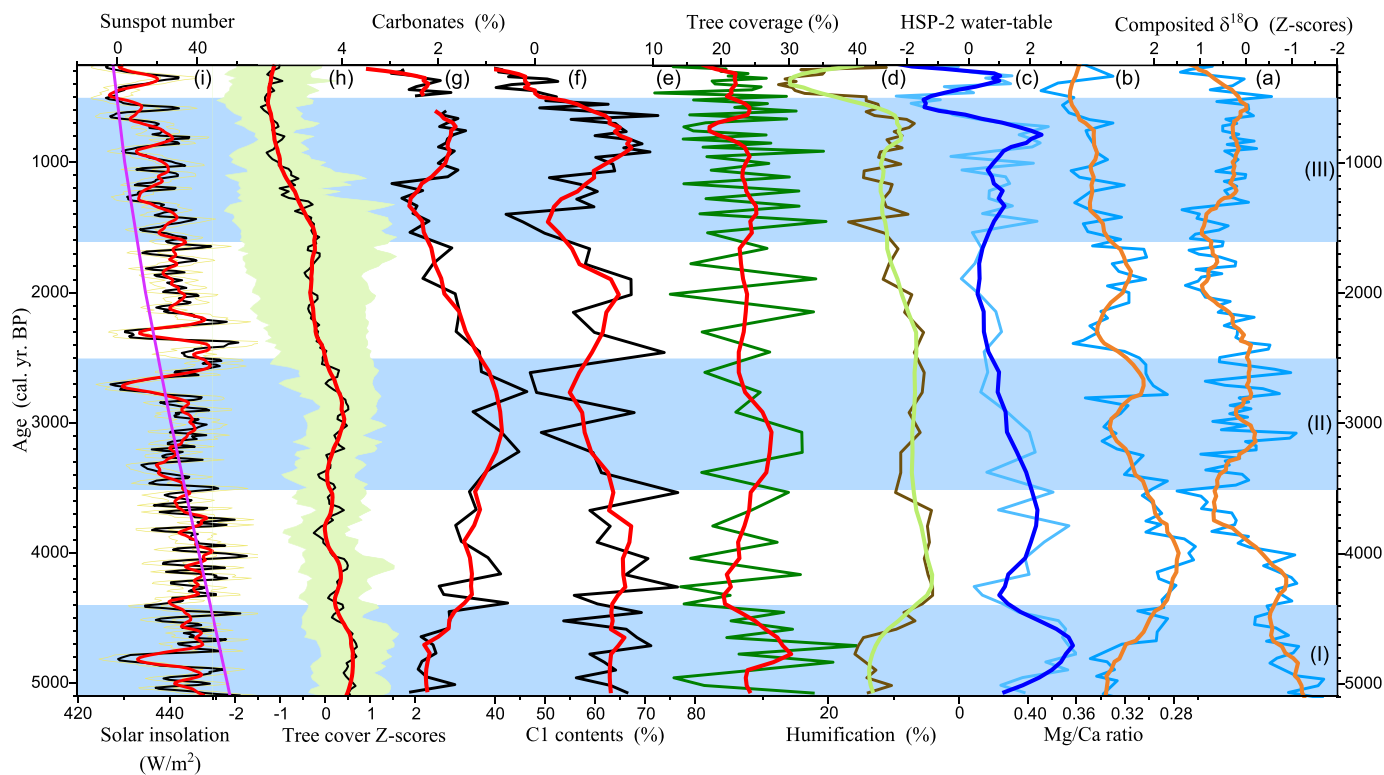


Fig. 11. Comparisons of the Hongshupao peatland paleo-records with regional and global paleoclimate profiles and solar forcing. (a) composited stalagmite $\delta^{18}\text{O}$ record for northeastern Asia (Zhao et al., 2021); (b) Mg/Ca ratio of Lake Dali sediments (Fan et al., 2016); (c) diatom-derived water-table reconstructions for the Hongshupao peatland (Li et al., 2020a); (d) HSP-2 humification profile (this study); (e) phytolith-based canopy coverage reconstruction (this study); (f) fine-grained ($<32\ \mu\text{m}$) component (C1) contents (this study); (g) HSP-2 carbonate profile (this study); (h) stacked tree pollen Z-scores along the East Asian monsoon margin (this study); (i) solar irradiation in July at 65°N (Berger and Loutre, 1991) and cosmic isotope based sunspot number reconstructions (Solanki et al., 2004).

Moreover, sedimentary and geochemical investigations have suggested that fine-grained mineral sediments have higher $\text{Al}_2\text{O}_3/\text{SiO}_2$ ratios, which usually indicate intensified chemical weathering, whereas coarse-grained sediments have lower $\text{Al}_2\text{O}_3/\text{SiO}_2$ ratios, typically corresponding to limited chemical weathering (e.g., Liu and Deng, 2014; Hatano et al., 2019). We deduce that the fine-grained mineral sediment in peat core HSP-2 originated from regional chemical weathering. Under warm and/or humid climates, more fine-grained clasts were produced by earth surface weathering, and this eventually resulted in high percentages of fine-grained mineral clasts in the studied core (Fig. 11).

(2) Climatic significance of humification

Peat humification is an indicator of peat breakdown or decomposition (Chambers et al., 2011). Because the principal reaction mechanism governing peat humification is oxidative degradation (Zaccone et al., 2018), parameters (e.g., temperature, wetness, pH, age) that alter the oxidative condition in a peatland could be reconstructed by determining the degree of humification of peaty samples (Chambers et al., 2011). Temperature and wetness are the most commonly reported factors that regulate the decomposition of peat (e.g., Chambers et al., 2011; Huang et al., 2013; Zaccone et al., 2018 and references therein). The degree of peat humification can be used to infer local or regional climate change (e.g., Huang et al., 2013). In northeastern Asia, peat humification is believed to be related to the intensity of the East Asian summer monsoon, specifically temperature and peatland wetness (Huang et al., 2013 and references therein). Considering covariation between the diatom-based water-table reconstructions and the humification profiles (Fig. 11) from the Hongshupao peatland in the present study, it is proposed that humification is regulated by local peatland conditions (temperature and local wetness) that were directly and/or indirectly related to regional climate change. The degree of humification in peat should be greater during warm and wet intervals (Huang et al., 2013).

4.2.2. Response of tree coverage to mid-Holocene climate change in the northern monsoon margin area

The phytolith-based tree coverage estimates reported in this study generally align with the physical and chemical proxy-inferred mid-Holocene hydro-climatic variations, indicating vegetation-climate feedbacks in the monsoon margins. Multiple lines of evidence from the Hongshupao peatland indicate that the interval from 5100 to 4400 cal. yr BP (stage I in Fig. 11) experienced warm and wet conditions (Fig. 11). The diatom-based reconstruction shows an elevated water table, and the carbonate content in the peat displays a decreasing trend, indicating decreased evaporation from the peatland surface (Fig. 11.c). During the same stage, $\delta^{18}\text{O}$ of most Chinese stalagmites are negative (Dong et al., 2010), suggesting an intensified East Asian summer monsoon in China (Dong et al., 2010; Jo et al., 2017; Zhao et al., 2021). The composited $\delta^{18}\text{O}$ record in northeastern Asia is also negative, pointing to a relatively humid stage (Jo et al., 2017; Zhao et al., 2021). The Mg/Ca ratio of the sediments in Lake Dali, likewise in the East Asian monsoon margin (Fig. 1A), is lower during the same period further reflecting conditions of depressed evaporation (Fan et al., 2016), possibly due to an increase in regional precipitation. The favorable climate within this stage supported plenty of trees and consequently resulted in greater canopy coverages (Fig. 10). A quick but profound dry interval, however, is recorded in the Hongshupao peatland. Approximately 4200–4300 cal. yr BP, the water table of the peatland fell sharply (Fig. 11.c, Li et al., 2020a). This was accompanied by a decrease in fine-grained minerals and an increase in carbonate content (Fig. 11.f), suggesting conditions of depressed weathering and greater evaporation. The phytolith frequency diagram (relative abundance) does not reflect this sudden vegetation succession (Fig. 4a). However, the absolute phytolith abundance, as expressed by phytolith concentration, decreased to 0.6×10^6 grains/g (phytolith influx declined to 0.8×10^4 grains/cm²/yr, Fig. 4b and c). This sudden

dry interval is also evidenced by the phytolith-based tree cover estimates (Fig. 11e), indicating a quick response of vegetation to climate deterioration: grass that could cope better with dryness expanded and tree coverage decreased (Woodward et al., 2004; Pan et al., 2013). This profound dry interval is comparable, and may be related, to the globally reported ‘4.2 ka event’ (e.g., Railsback et al., 2018; Xiao et al., 2018; Bini et al., 2019; Scuderi et al., 2019), suggesting that the climate shifts observed in HSP-2 records are related to regional climate variations rather than peatland-specific conditions.

After the ‘4.2 ka event,’ regional tree coverage increased slightly, peaking around 3200–3100 cal. yr BP. Afterward, the regional tree coverage displayed a generally decreasing trend and then fluctuated (Fig. 11). The interval from 3500 to 2500 cal. yr BP represents another stage of dense canopy coverage (stage II in Fig. 11). This period of increased canopy coverage might be linked to the short climate amelioration that is evidenced by decreasing Mg/Ca ratios in Lake Dali sediments from 2800 to 2500 cal. yr BP (Fan et al., 2016) and the negative shifts of the composited stalagmite $\delta^{18}\text{O}$ record in northeastern Asia (Zhao et al., 2021). Carbonate content of the peat has the lowest values in the section during 3200–2700 cal. yr BP (Fig. 11), pointing to a wetter episode in the overall drying trend (Jones and Bowser, 1978; Fan et al., 2019).

During the last two millennia, regional canopy coverage surrounding the peatland increased again (stage III: 1600–500 cal. yr BP). In the Hongshupao peatland, biotic and abiotic proxies suggest climate improvement since 1600 cal. yr BP (Fig. 11c). The diatom evidence points to an elevated water table starting about 1600 cal. yr BP that lasted for almost 800 years, and the carbonates in HSP-2 decreased after 1100 cal. yr BP (Fig. 11g). Fine mineral grains (C1) likewise indicate this trend, with increased percentages from 1300 cal. yr BP (Fig. 11f). The higher percentages of fine-grained sediments during 900 to 600 cal. yr BP (ca. 1050–1350 CE) suggest an increase in chemical weathering. As a response to regional climate amelioration, the phytolith-estimated tree cover increased during this interval (Fig. 11e). Chronologically, this wet interval is consistent with the medieval warm period (MWP) that has been widely reported in Europe (e.g., Lamb, 1965) and parts of Asia (e.g., Zhu, 1973). In northeastern Asia, this wetter period is evidenced by a negative shift in stalagmite $\delta^{18}\text{O}$ values (Zhao et al., 2021). The MWP-like event, however, is not reflected in the Mg/Ca ratios of Lake Dali sediments of northern China (Fan et al., 2016) or the speleothem $\delta^{18}\text{O}$ curves from Sanbao Cave in central China (Dong et al., 2010). This discrepancy between records from northern China and northeastern China may imply that the climate history and associated vegetation feedbacks have differed among sub-bioclimatic zones in the East Asian monsoon region during the past two millennia. This hypothesis, however, needs further investigation. The MWP-like climate event ended about 600 cal. yr BP., after which the regional climate started to deteriorate again (Fig. 11).

In summary, in response to the Holocene northern hemisphere insolation variations (Berger and Loutre, 1991), regional climate in the monsoon margin area has experienced a generally deteriorating trend since the mid-Holocene (Dong et al., 2010; Yin et al., 2013; Hao et al., 2014; Liu et al., 2014; Xiao et al., 2018; Fan et al., 2019; Wu et al., 2019; Zhao et al., 2021). Despite discrepancies, the multiple proxy-based paleoclimate reconstruction is generally consistent with the well-recognized evolution of the East Asian monsoon. The timing, structure, and amplitude of climate events are comparable to those within the monsoon-influenced core area and/or to global climate shifts. As a response, vegetation coverage, as well as its composition, changed as the climate shifted.

4.3. Importance of precipitation in regulating vegetation change in the monsoon margin area

Almost all proxy-based reconstructions incorporate both temperature and precipitation effects; impacts of variations in temperature or

precipitation on terrestrial ecosystems have seldom been determined in proxy-based reconstructions. Dynamic global vegetation models (DGVMs), however, allow us to evaluate and observe the sensitivity of terrestrial vegetation to change in a single climatic parameter (Reitalu et al., 2013; Lu et al., 2018).

LPJ-GUESS simulations show that distribution and variation of forest/steppe cover are sensitive to precipitation rather than temperature (Figs. 7 and 8). Present ecological understanding indicates that precipitation is one of the main factors limiting the growth of woody and herbaceous communities (Woodward et al., 2004; Pan et al., 2013). In arid and semiarid lands, ecological and physiological observations of modern vegetation have suggested that, compared with temperature, precipitation patterns and amounts have greater potential to induce plant productivity, composition, and diversity changes (e.g., Bates et al., 2006 and references therein). Precipitation is a more direct, mechanistic factor than temperature in regulating forest distribution (Woodward et al., 2004; Pan et al., 2013) because trees have higher transpiration needs than grasses (Pan et al., 2013). Grasses prevail over trees in drier conditions because they have a particularly strong competitive advantage over tree seedlings (e.g., Higgins et al., 2012; Pan et al., 2013; Baudena et al., 2015). Globally, the distribution of different biomes corresponds primarily to the geographical distribution of climate, implying a correlation between the biomes and climatic conditions (Woodward et al., 2004; Pan et al., 2013). In northeastern China, vegetation distribution along an east-west transect is primarily influenced by the precipitation gradient (Ni and Zhang, 2000). The modern vegetation transition from forest in the east to typical steppe in the west reveals the vegetation response to precipitation variations under similar mean annual temperatures, demonstrating the role of precipitation in modulating vegetation change for the study region and adjacent areas (Ni and Zhang, 2000).

In addition to modern observations, increasing evidence from geological records have shown that in arid and semiarid ecosystems, precipitation exerts a primary control on regional vegetation distribution and dynamics (e.g., Liu and Yin, 2013; Yin et al., 2013; Hao et al., 2014; Liu et al., 2014; Zhao et al., 2017). For instance, employing multiple proxy-based reconstructions, Li et al. (2021) reported that a continuous aridification trend since the mid-Holocene is the main driver of variations in relative abundance of C3/C4 species in the Songnen plain of northeastern China, indicating the importance of precipitation in modulating regional vegetation dynamics.

In conclusion, both comprehensive DGVM simulations and field surveys reveal that precipitation is a key factor regulating vegetation dynamics in the arid and semiarid lands of northeastern China, and this is also supported by the precipitation threshold hypothesis for arid lands (Scheffer et al., 2001; Zhao et al., 2017). If climate continues to control monsoon margin vegetation composition, further changes in this ecosystem can be expected to accompany the projected future warming and associated precipitation anomaly.

5. Conclusions

This study presents new phytolith-based paleovegetation composition and quantitative canopy coverage reconstructions in the East Asian monsoon margin area. Employing multiple proxy-based evidence, we provide an improved understanding of vegetation responses to past (or future) climate change. Phytolith-based vegetation reconstruction revealed a general decreasing trend of tree coverage and shifts in dominant plant communities, largely consistent with peat textural composition and geochemical proxy profiles, which suggest a decrease in regional precipitation since 5100 cal. yr BP. These results agree with other geological records in East Asia, underscoring the controlling role of the East Asian monsoon on regional vegetation change. As reflected in variations in tree coverage and dominant plant communities, monsoon margin vegetation responds rapidly to long-term climate shifts. Variation partitioning suggests that monsoon climate variation is most likely

responsible for the vegetation change, emphasizing the role of precipitation in regulating monsoon margin vegetation dynamics. The dominant role of precipitation is further validated by simulating different scenarios using the dynamic global vegetation model (LPJ-GUESS).

Data availability statement

All data supporting the main findings of this study will be available online as supplementary materials to this article.

Declaration of Competing Interest

None.

Acknowledgments

This work was financially supported by the National Natural Science Foundation of China (Grant No. 41771214, 42001075, 41971100), the National Key Research and Development Project of China (Grant No. 2016YFA0602301), China Postdoctoral Science Foundation (Grant No. 2021M691862), and the Outstanding Postdoctoral Scholarship of the State Key Laboratory of Marine Environmental Science at Xiamen University. Zhengyao Lu received funding from FORMAS mobility (Grant No. 2020-02267). Dr. Xin Xu from Institute of Atmospheric Physics (CAS) is acknowledged for kindly providing the synthesized paleofire data.

Appendix A. Supplementary data

Supplementary data to this article can be found online at <https://doi.org/10.1016/j.palaeo.2022.110842>.

References

- Aleman, J.C., Canal-Subitani, S., Favier, C., Bremond, L., 2014. Influence of the local environment on lacustrine sedimentary phytolith records. *Palaeogeogr. Palaeoclimatol. Palaeoecol.* 414, 273–283.
- Alexandre, A., Meunier, J.-D., Lézine, A.-M., Vincens, A., Schwartz, D., 1997. Phytoliths: indicators of grassland dynamics during the late Holocene in intertropical Africa. *Palaeogeogr. Palaeoclimatol. Palaeoecol.* 136, 213–229.
- Barboni, D., Bremond, L., 2009. Phytoliths of East African grasses: an assessment of their environmental and taxonomic significance based on floristic data. *Rev. Palaeobot. Palynol.* 158, 29–41.
- Barboni, D., Bonnefille, R., Alexandre, A., Meunier, J.D., 1999. Phytoliths as paleoenvironmental indicators, West Side Middle Awash Valley, Ethiopia. *Palaeogeogr. Palaeoclimatol. Palaeoecol.* 152, 87–100.
- Bates, J.D., Svejcar, T., Miller, R.F., Angell, R.A., 2006. The effects of precipitation timing on sagebrush steppe vegetation. *J. Arid Environ.* 64, 670–697.
- Baudena, M., Dekker, S.C., van Bodegom, P.M., Cuesta, B., Higgins, S.I., Lehsten, V., Reick, C.H., Rietkerk, M., Scheiter, S., Yin, Z., Zavala, M.A., Brovkin, V., 2015. Forests, savannas, and grasslands: bridging the knowledge gap between ecology and dynamic global vegetation models. *Biogeosciences* 12, 1833–1848.
- Berger, A., Loutre, M.F., 1991. Insolation values for the climate of the last 10 million years. *Quat. Sci. Rev.* 10, 297–317.
- Bini, M., Zanchetta, G., Persio, A., Cartier, R., Català, A., Cacho, I., Dean, J.R., Di Rita, F., Drysdale, R.N., Finnè, M., Isola, I., Jalali, B., Lirer, F., Magri, D., Masi, A., Marks, L., Mercuri, A.M., Peyron, O., Sadori, L., Sicre, M.-A., Welc, F., Zielhofer, C., Brisset, E., 2019. The 4.2 ka BP event in the Mediterranean region: an overview. *Clim. Past* 15, 555–577.
- Boulay, S., Colin, C., Trentesaux, A., Pluquet, F., Bertaux, J., Blamart, D., Buehring, C., Wang, P., 2003. Mineralogy and sedimentology of Pleistocene sediment in the South China Sea (ODP Site 1144). *Proc. Ocean Drill. Program Sci. Results* 184, 1–21.
- Boyd, M., 2005. Phytoliths as paleoenvironmental indicators in a dune field on the northern Great Plains. *J. Arid Environ.* 61, 357–375.
- Bremond, L., Alexandre, A., Wooller, M.J., Hély, C., Williamson, D., Schäfer, P.A., Majule, A., Guiot, J., 2008. Phytolith indices as proxies of grass subfamilies on East African tropical mountains. *Glob. Planet. Chang.* 61, 209–224.
- Chambers, F.M., Beilman, D.W., Yu, Z., 2011. Methods for determining peat humification and for quantifying peat bulk density, organic matter and carbon content for palaeostudies of climate and peatland carbon dynamics. *Mires Peat* 7, 1–10. Article 7.
- Chen, F., Xu, Q., Chen, J., Birks, J.H.B., Liu, J., Zhang, S., Jin, L., An, C., Telford, R.J., Cao, X., Wang, Z., Zhang, X., Selvaraj, K., Lu, H., Li, Y., Zheng, Z., Wang, H., Zhou, A., Dong, G., Zhang, J., Huang, X., Bloemendal, J., Rao, Z., 2015. East Asian summer monsoon precipitation variability since the last deglaciation. *Sci. Rep.* 5, 11186. <https://doi.org/10.1038/srep11186>.
- Cheng, Y., Liu, H., Dong, Z., Duan, K., Wang, H., Han, Y., 2020. East Asian summer monsoon and topography co-determine the Holocene migration of forest-steppe ecotone in northern China. *Glob. Planet. Chang.* 187, 103135.
- China Meteorological Data Service Center, 2020. Monthly Averaged Climate Data of A'er'shan Meteorological Station (1981 to 2010). China Meteorological Data Service Center. <http://data.cma.cn/>.
- Cui, Q., Zhao, Y., Qin, F., Liang, C., Li, Q., Geng, R., 2019. Characteristics of the modern pollen assemblages from different vegetation zones in Northeast China: implications for pollen-based climate reconstruction. *Sci. China Earth Sci.* 62 (10), 1564–1577.
- Dong, J., Wang, Y., Cheng, H., Hardt, B., Edwards, R.L., Kong, X., Wu, J., Chen, S., Liu, D., Jiang, X., Zhao, K., 2010. A high-resolution stalagmite record of the Holocene East Asian monsoon from Mt Shennongjia, central China. *Holocene* 20, 257–264.
- Erdős, L., Ambarli, D., Anenkhonov, O.A., Bátori, Z., Cserhalmi, D., Kiss, M., Kröel-Dulay, G., Liu, H., Magnes, M., Molnár, Z., Naqinezhad, A., Semenishchenkov, Y.A., Tölgysesi, C., 2018. The edge of two worlds: a new review and synthesis on Eurasian forest-steppes. *Appl. Veg. Sci.* 21 (3), 345–362.
- Fan, J., Xiao, J., Wen, R., Zhang, S., Wang, X., Cui, L., Li, H., Xue, D., Yamagata, H., 2016. Droughts in the East Asian summer monsoon margin during the last 6 kyrs: link to the North Atlantic cooling events. *Quat. Sci. Rev.* 151, 88–99.
- Fan, J., Xiao, J., Wen, R., Zhang, S., Huang, Y., Yue, J., Wang, X., Cui, L., Li, H., Xue, D., Liu, Y., 2019. Mineralogy and carbonate geochemistry of the Dali Lake sediments: implications for paleohydrological changes in the East Asian summer monsoon margin during the Holocene. *Quat. Int.* 527, 103–112.
- Gao, G., Jie, D., Li, D., Li, N., Liu, L., Liu, H., Shi, J., Leng, C., Wang, J., Liu, B., Li, P., 2018a. Reliability of phytoliths for reconstructing vegetation dynamics in northern temperate forest regions: a case study in northeast China. *Quat. Sci. Rev.* 201, 1–12.
- Gao, G., Jie, D., Wang, Y., Liu, L., Liu, H., Li, D., Li, N., Shi, J., Leng, C., 2018b. Phytolith reference study for identifying vegetation changes in the forest-grassland region of northeast China. *Boreas* 47, 481–497.
- Grimm, E.C., 1987. CONISS: a Fortran 77 program for stratigraphically constrained cluster analysis by the method of the incremental sum of squares. *Comput. Geosci.* 13, 13–35.
- Grimm, E.C., 1992. TILIA and TILIA*GRAPH Computer Program. Illinois State Museum, Springfield, IL.
- Hansen, M.C., Potapov, P.V., Moore, R., Hancher, M., Turubanova, S.A., Tyukavina, A., Thau, D., Stehman, S.V., Goetz, S.J., Loveland, T.R., Kommareddy, A., Egorov, A., Chini, L., Justice, C.O., Townsend, J.R.G., 2013. High-resolution global maps of 21st-century forest cover change. *Science* 342, 850–853.
- Hao, Q., Liu, H., Yin, Y., Wang, H., Feng, M., 2014. Varied responses of forest at its distribution margin to Holocene monsoon development in northern China. *Palaeogeogr. Palaeoclimatol. Palaeoecol.* 409, 239–248.
- Hatano, N., Yoshida, K., Sasao, E., 2019. Effects of grain size on the chemical weathering index: a case study of Neogene fluvial sediments in southwest Japan. *Sediment. Geol.* 386, 1–8.
- Hazeleger, W., Severijns, C., Semmler, T., Ştefanescu, S., Yang, S., Wang, X., Wyser, K., Dutra, E., Baldasano, J.M., Bintanja, R., Bougeault, P., Caballero, R., Ekman, A.M.L., Christensen, J.H., van den Hurk, B., Jimenez, P., Jones, C., Källberg, P., Koenigk, T., McGrath, R., Miranda, P., van Noije, T., Palmer, T., Parodi, J.A., Schmitt, T., Selten, F., Storelmyr, T., Sterl, A., Tapamo, H., Vancoppenolle, M., Viterbo, P., Willén, U., 2010. EC-Earth: a seamless earth-system prediction approach in action. *Bull. Am. Meteorol. Soc.* 91, 1357–1363.
- Higgins, S.I., Bond, W.J., Combrink, H., Craine, J.M., February, E.C., Govender, N., Lannas, K., Moncreiff, G., Trollope, W.S.W., 2012. Which traits determine shifts in the abundance of tree species in a fire-prone savanna? *J. Ecol.* 100, 1400–1410.
- Hou, X., 1982. Vegetation Geography of China and Chemical Components of Their Dominant Plants. Science Press, Beijing, pp. 1–411 (in Chinese).
- Huang, T., Cheng, S., Mao, X., Hong, B., Hu, Z., Zhou, Y., 2013. Humification degree of peat and its implications for Holocene climate change in Hani peatland, Northeast China. *Chin. J. Geochem.* 32, 406–412.
- International Committee for Phytolith Taxonomy (ICPT), 2019. International Code for Phytolith Nomenclature (ICPN) 2.0. *Ann. Bot.* 124 (2), 189–199.
- Jiang, W., Guo, Z., Sun, X., Wu, H., Chu, G., Yuan, B., Hatté, C., Guiot, J., 2006. Reconstruction of climate and vegetation changes of Lake Bayanchagan (Inner Mongolia): Holocene variability of the East Asian monsoon. *Quat. Res.* 65, 411–420.
- Jo, K., Yi, S., Lee, J.-Y., Woo, K.S., Cheng, H., Edwards, L.R., Kim, S.-T., 2017. 1000-year quasi-periodicity of weak monsoon events in temperate northeast Asia since the mid-holocene. *Sci. Rep.* 7, 15196. <https://doi.org/10.1038/s41598-017-15566-4>.
- Jones, B.F., Bowser, C.J., 1978. The mineralogy and related chemistry of lake sediments. In: Lerman, A. (Ed.), Lakes: Chemistry, Geology, Physics. Springer, New York, pp. 179–235.
- Juggins, S., 2020. Rioja: Analysis of Quaternary Science Data. R package version 0.9-26. <https://cran.r-project.org/package=rioja>.
- Kondo, R., Childs, C., Atkinson, I., 1994. Opal Phytoliths of New Zealand. Manaaki Whenua Press, Lincoln.
- Kukla, T., Ahlström, A., Maezumi, S.Y., Chevalier, M., Lu, Z., Winnick, M.J., Chamberlain, C.P., 2021. The resilience of Amazon tree cover to past and present drying. *Glob. Planet. Chang.* 202, 103520.
- Lamb, H.H., 1965. The early medieval warm epoch and its sequel. *Palaeogeogr. Palaeoclimatol. Palaeoecol.* 1 (65), 13–37.
- Li, Y., Zhang, X., Zhou, G., 2000. Quantitative relationships between vegetation and several pollen taxa in surface soil from North China. *Chin. Sci. Bull.* 45 (16), 1519–1523.
- Li, Y., Bunting, M.J., Xu, Q., Jiang, S., Ding, W., Hun, L., 2011. Pollen–vegetation–climate relationships in some desert and desert-steppe communities in northern China. *Holocene* 21 (6), 997–1010.

- Li, N., Sack, D., Gao, G., Liu, L., Li, D., Yang, X., Jie, D., Liu, H., Shi, J., Leng, C., 2018. Holocene *Artemisia-Chenopodiaceae*-dominated grassland in North China: real or imaginary? *Holocene* 28, 834–841.
- Li, N., Li, M., Sack, D., Kang, W., Song, L., Yang, Y., Zong, Y., Jie, D., 2020a. Diatom evidence for mid-Holocene peatland water-table variations and their possible link to solar forcing. *Sci. Total Environ.* 725, 138272.
- Li, N., Sack, D., Sun, J., Liu, S., Liu, B., Wang, J., Gao, G., Li, D., Song, Z., Jie, D., 2020b. Quantifying the carbon content of aeolian sediments: which method should we use? *Catena* 185, 104276.
- Li, N., Xie, M., Sack, D., Dubois, N., Yang, X., Gao, G., Li, D., Liu, L., Liu, H., Leng, C., Wang, J., Liu, B., Jie, D., 2021. Continuous aridification since the mid-Holocene as the main cause of C_3/C_4 dynamics in the grasslands of northeastern China. *Eur. J. Soil Sci.* 72, 356–371.
- Liu, C., Deng, C., 2014. The effect of weathering on the grain-size distribution of red soils in south-eastern China and its climatic implications. *J. Asian Earth Sci.* 94, 94–104.
- Liu, H., Xu, L., Cui, H., 2002. Holocene history of desertification along the woodland-steppe border in northern China. *Quat. Res.* 57, 259–270.
- Liu, H., Yin, Y., 2013. Response of forest distribution to past climate change: an insight into future predictions. *Chin. Sci. Bull.* 58, 4426–4436.
- Liu, Z., Otto-Blieneser, B.L., He, F., Brady, E.C., Tomas, R., Clark, P.U., Carlson, A.E., Lynch-Stieglitz, J., Curry, W., Brook, E., Erickson, D., Jacob, R., Kutzbach, J., Cheng, J., 2009. Transient simulation of deglacial climate evolution with a new mechanism for Bolling-Allerod warming. *Science* 325, 310–314.
- Liu, H., He, S., Anenkovon, O.A., Hu, G., Sandanov, D.V., Badmaeva, N.K., 2012. Topography-controlled soil water content and the coexistence of forest and steppe in Northern China. *Phys. Geogr.* 33 (6), 561–573.
- Liu, H., Yin, Y., Hao, Q., Liu, G., 2014. Sensitivity of temperate vegetation to Holocene development of East Asian monsoon. *Quat. Sci. Rev.* 98, 126–134.
- Liu, H., Wu, N., Yang, X., Jiang, H., Liu, K., Liu, T., 2006. Phytoliths as quantitative indicators for the reconstruction of past environmental conditions in China: phytolith based transfer functions. *Quat. Sci. Rev.* 25, 945–959.
- Lu, Z., Miller, P.A., Zhang, Q., Zhang, Q., Wärnlund, D., Nieradzik, L., Sjolte, J., Smith, B., 2018. Dynamic vegetation simulations of the mid-Holocene Green Sahara. *Geophys. Res. Lett.* 45, 8294–8303.
- Liu, H., Yin, Y., Zhu, J., Zhao, F., Wang, H., 2010. How did the forest respond to Holocene climate drying at the forest-steppe ecotone in northern China? *Quat. Int.* 227, 46–52.
- Lu, Z., Miller, P.A., Zhang, Q., Wärnlund, D., Nieradzik, L., Sjolte, J., Li, Q., Smith, B., 2019. Vegetation pattern and terrestrial carbon variation in past warm and cold climates. *Geophys. Res. Lett.* 46, 8133–8143.
- Lucht, W., Schaphoff, S., Erbrecht, T., Heyder, U., Cramer, W., 2006. Terrestrial vegetation redistribution and carbon balance under climate change. *Carbon Balance Manag.* 1 (1), 6. <https://doi.org/10.1186/1750-0680-1-6>.
- Neumann, K., Fahmy, A.G., Müller-Scheefel, N., Schmidt, M., 2017. Taxonomic, ecological and palaeoecological significance of leaf phytoliths in West African grasses. *Quat. Int.* 434, 15–32.
- Ni, J., Zhang, X., 2000. Climate variability, ecological gradient and the Northeast China Transect (NECT). *J. Arid Environ.* 46, 313–325.
- Oksanen, J., Blanchet, F.G., Friendly, M., Kindt, R., Legendre, P., McGlinn, D., Minchin, P.R., O'Hara, R.B., Simpson, G.L., Solymos, P., Stevens, M.H.H., Szoecs, E., Wagner, H., 2020. vegan: Community Ecology Package. R package version 2.5–7. <https://CRAN.R-project.org/package=vegan>.
- Pan, Y., Birdsey, R.A., Phillips, O.L., Jackson, R.B., 2013. The structure, distribution, and biomass of the world's forests. *Annu. Rev. Ecol. Evol. Syst.* 44, 593–622.
- Pausata, F.S., Messori, G., Zhang, Q., 2016. Impacts of dust reduction on the northward expansion of the African monsoon during the Green Sahara period. *Earth Planet. Sci. Lett.* 434, 298–307.
- Piperno, D.R., 1988. Phytolith Analysis. An Archaeological and Geological Perspective. Academic Press, New York.
- Poorter, H., Navas, M.L., 2003. Plant growth and competition at elevated CO₂: on winners, losers and functional groups. *New Phytol.* 157 (2), 175–198.
- Qian, H., Yuan, X., Chou, Y., 2003. Forest vegetation of northeast China. In: Kolbek, J., Šrútek, M., Box, Elgene O. (Eds.), *Forest Vegetation of Northeast Asia*. Springer, Dordrecht, pp. 181–230.
- R Core Team, 2020. R: A Language and Environment for Statistical Computing. R Foundation for Statistical Computing, Vienna, Austria. <https://www.R-project.org>.
- Railsback, L.B., Liang, F., Brook, G.A., Voarintsoa, N.R.G., Sletten, H.R., Marais, E., Hardt, B., Edwards, R.L., 2018. The timing, two-pulsed nature, and variable climatic expression of the 4.2 ka event: a review and new high-resolution stalagmite data from Namibia. *Quat. Sci. Rev.* 186, 78–90.
- Reitalu, T., Seppä, H., Sugita, S., Kangur, M., Koff, T., Avel, E., Kihno, K., Vassiljev, J., Renssen, H., Hammarlund, D., Heikkilä, M., Saarse, L., Poska, A., Veski, S., 2013. Long-term drivers of forest composition in a boreonemoral region: the relative importance of climate and human impact. *J. Biogeogr.* 40, 1524–1534.
- RStudio Team, 2020. RStudio: Integrated Development Environment for R. RStudio, Inc., Boston, MA. <http://www.rstudio.com>.
- Scheffer, M., Carpenter, S., Foley, J.A., Folke, C., Walker, B., 2001. Catastrophic shifts in ecosystems. *Nature* 413, 591–596.
- Scuderi, L.A., Yang, X., Ascoli, S.E., Li, H., 2019. The 4.2 ka BP Event in northeastern China: a geospatial perspective. *Clim. Past* 15, 367–375.
- Shotyk, W., 1988. Review of the inorganic geochemistry of peats and peatland waters. *Earth Sci. Rev.* 25, 95–176.
- Smith, B., Prentice, I.C., Sykes, M.T., 2001. Representation of vegetation dynamics in modelling of terrestrial ecosystems: comparing two contrasting approaches within European climate space. *Glob. Ecol. Biogeogr.* 10, 621–637.
- Smith, B., Wärnlund, D., Arneth, A., Hickler, T., Leadley, P., Siltberg, J., Zaehle, S., 2014. Implications of incorporating N cycling and N limitation on primary production in an individual-based dynamic vegetation model. *Biogeosciences* 11, 2027–2054.
- Solanki, S.K., Usoskin, I.G., Kromer, B., Schüssler, M., Beer, J., 2004. Unusual activity of the Sun during recent decades compared to the previous 11,000 years. *Nature* 431, 1084–1087.
- Stebich, M., Rehfeld, K., Schlüter, F., Tarasov, P.E., Liu, J., Mingram, J., 2015. Holocene vegetation and climate dynamics of NE China based on the pollen record from Sihailongwan Maar Lake. *Quat. Sci. Rev.* 124, 275–289.
- Strömborg, C.A.E., 2004. Using phytolith assemblages to reconstruct the origin and spread of grass-dominated habitats in the Great Plains of North America during the late Eocene to early Miocene. *Palaeogeogr. Palaeoclimatol. Palaeoecol.* 207, 239–275.
- Sun, A., Feng, Z., 2013. Holocene climatic reconstructions from the fossil pollen record at Qigai Nuur in the southern Mongolian Plateau. *Holocene* 23, 1391–1402.
- Turner, M.G., Wei, D., Prentice, I.C., Harrison, S.P., 2021. The impact of methodological decisions on climate reconstructions using WA-PLS. *Quat. Res.* 99, 341–356.
- Twiss, P.C., 1992. Predicted world distribution of C3 and C4 grass phytoliths. In: Rapp, G.R., Mulholland, S.C. (Eds.), *Phytoliths systematics: emerging issues*. Advance Archaeological Museum Science, 1. Plenum Press, New York, pp. 113–128.
- Twiss, P.C., Suess, E., Smith, R.M., 1969. Morphological classification of grass phytoliths. *Soil Sci. Soc. Am. J.* 33, 109–115.
- Wang, H., Liu, H., Zhu, J., Yin, Y., 2010. Holocene environmental changes as recorded by mineral magnetism of sediments from Anguli-nuur Lake, southeastern Inner Mongolia Plateau, China. *Palaeogeogr. Palaeoclimatol. Palaeoecol.* 285, 30–49.
- Wang, Y., Lu, H., 1993. The Study of Phytolith and its Application. China Ocean Press, Beijing (in Chinese).
- Wen, R., Xiao, J., Chang, Z., Zhai, D., Xu, Q., Li, Y., Itoh, S., 2010. Holocene precipitation and temperature variations in the East Asian monsoonal margin from pollen data from Hulun Lake in northeastern Inner Mongolia, China. *Boreas* 39, 262–272.
- Wen, R., Xiao, J., Fan, J., Zhang, S., Yamagata, H., 2017. Pollen evidence for a mid-Holocene East Asian summer monsoon maximum in northern China. *Quat. Sci. Rev.* 176, 29–35.
- Woodward, F.I., Lomas, M.R., Kelly, C.L., 2004. Global climate and the distribution of plant biomes. *Philos. Trans. R. Soc. Lond. B Biol. Sci.* 359, 1465–1476.
- Wu, J., Liu, Q., Cui, Q., Xu, D., Wang, L., Shen, C., Chu, G., Liu, J., 2019. Shrinkage of East Asia Winter Monsoon associated with increased ENSO events since the mid-Holocene. *J. Geophys. Res. Atmos.* 24, 3839–3848.
- Xiao, J., Xu, Q., Nakamura, T., Yang, X., Liang, W., Inouchi, Y., 2004. Holocene vegetation variation in the Dihai Lake region of north-central China: a direct indication of the Asian monsoon climatic history. *Quat. Sci. Rev.* 23, 1669–1679.
- Xiao, J., Zhang, S., Fan, J., Wen, R., Zhai, D., Tian, Z., Jiang, D., 2018. The 4.2 ka BP event: multi-proxy records from a closed lake in the northern margin of the East Asian summer monsoon. *Clim. Past* 14, 1417–1425.
- Xu, Q., Li, Y., Yang, X., Zheng, Z., 2007. Quantitative relationship between pollen and vegetation in northern China. *Sci. China Ser. D Earth Sci.* 50 (4), 582–599.
- Xu, Q., Cao, X., Tian, F., Zhang, S., Li, Y., Li, M., Li, J., Liu, Y., Liang, J., 2014. Relative pollen productivities of typical steppe species in northern China and their potential in past vegetation reconstruction. *Sci. China Earth Sci.* 57, 1254–1266.
- Xu, D., Lu, H., Chu, G., Liu, L., Shen, C., Li, F., Wang, C., Wu, N., 2019. Synchronous 500-year oscillations of monsoon climate and human activity in Northeast Asia. *Nat. Commun.* 10, 4105.
- Xu, X., Li, F., Lin, Z., Song, X., 2021. Holocene fire history in China: responses to climate change and human activities. *Sci. Total Environ.* 753, 142019.
- Yang, Z., 2001. Reconstruction of climate and environment since the Holocene in Diaojiaohai Lake Area, Daqing Mountains, Inner Mongolia. *Acta Ecol. Sin.* 21 (4), 538–543 (in Chinese).
- Yin, Y., Liu, H., Liu, G., Hao, Q., Wang, H., 2013. Vegetation responses to mid-Holocene extreme drought events and subsequent long-term drought on the southeastern Inner Mongolian Plateau, China. *Agric. For. Meteorol.* 178–179, 3–9.
- Zaccone, C., Plaza, C., Ciavatta, C., Miano, T.M., Shotyk, W., 2018. Advances in the determination of humification degree in peat since Achard (1786): applications in geochemical and paleoenvironmental studies. *Earth Sci. Rev.* 185, 163–178.
- Zhao, Y., Yu, Z., 2012. Vegetation response to Holocene climate change in East Asian monsoon-margin region. *Earth Sci. Rev.* 113, 1–10.
- Zhao, Y., Yu, Z., Chen, F., 2009. Spatial and temporal patterns of Holocene vegetation and climate changes in arid and semi-arid China. *Quat. Int.* 194, 6–18.
- Zhao, Y., Liu, Y., Guo, Z., Fang, K., Li, Q., Cao, X., 2017. Abrupt vegetation shifts caused by gradual climate changes in central Asia during the Holocene. *Sci. China Earth Sci.* 60, 1317–1327.
- Zhao, J., Tan, L., Yang, Y., Pérez-Mejías, C., Brahim, Y.A., Lan, J., Wang, J., Li, H., Wang, T., Zhang, H., Cheng, H., 2021. New insights towards an integrated understanding of NE Asian monsoon during mid to late Holocene. *Quat. Sci. Rev.* 254, 106793.
- Zhu, K., 1973. Preliminary study on climate change over last 5000 years in China. *Sci. China* 2, 168–189 (in Chinese).